V. Singh, R. Vescovini, R. Kumar, S.N. Patel, G. Watts
Nonlinear Vibration and Instability of a Randomly Distributed Cnt-Reinforced Composite Plate Subjected to Localized In-Plane Parametric Excitation
Applied Mathematical Modelling, In press - Published online 24/08/2021
doi:10.1016/j.apm.2021.08.018

Nonlinear Vibration and Instability of a Randomly Distributed CNT-Reinforced Composite Plate Subjected to Localized In-plane Parametric Excitation

Vishal Singh[1], R. Vescovini[2], Rajesh Kumar[3], S. N. Patel[4], Gaurav Watts[5]

[1]Research Scholar, Dept. of Civil Engineering, Birla Institute of Technology and Science Pilani, Pilani Campus, 333031, India. Email: p20180012@pilani.bits-pilani.ac.in

[2]Associate Professor, Dept. of Aerospace Engineering, Politecnico di Milano, Milano, Italy. Email: riccardo.vescovini@polimi.it

[3]Assistant Professor, Dept. of Civil Engineering, Birla Institute of Technology and Science Pilani, Pilani Campus, 333031, India (corresponding author). Email: rajesh.kr@pilani.bits-pilani.ac.in

[4]Assistant Professor, Dept. of Civil Engineering, Birla Institute of Technology and Science Pilani, Pilani Campus, 333031, India. Email: shuvendu@pilani.bits-pilani.ac.in

[5]Assistant Professor, Dept. of Mechanical Engineering, Birla Institute of Technology and Science Pilani, Pilani Campus, 333031, India. Email: gaurav.watts@pilani.bits-pilani.ac.in

Abstract: This study presents a semi-analytical formulation for the nonlinear vibration and dynamic instability of a randomly distributed carbon nanotube-reinforced composite (RD-CNTRC) plate. Three cases of localized in-plane periodic loadings are studied. The analytical stress fields within the RD-CNTRC plate for all the in-plane stress components (σ_{ij}, ($i, j = x, y$)) are developed by solving the in-plane elastic problem using Airy's stress approach. The effective mechanical properties of the RD-CNTRC plate are evaluated by the Eshelby-Mori-Tanaka technique. The plate is modeled based on higher-order shear deformation theory (HSDT) in conjunction with the von-Kármán nonlinearity. Using Hamilton's principle, the governing partial differential equations (PDEs) are derived, whose approximate solution is sought, referring to the Galerkin method. The resulting nonlinear ODEs are solved using the Incremental Harmonic Balance Method (IHB) to compute the nonlinear vibration response of the RD-CNTRC plate. Further dropping the nonlinear terms, these ODEs are solved by Bolotin's method to trace the instability region. The proposed semi-analytical method is an effective strategy for studying the influence of different parameters such as agglomeration models, CNT mass fraction, pre-loading, and boundary conditions on the nonlinear vibration and dynamic instability characteristics of the RD-CNTRC plates. The reduced computational effort allows the design phase to be supported in selecting parameters when designing RD-CNTRC plates with stability and vibration requirements.

Author Keywords: RD-CNTRC plate; localized in-plane loading; Eshelby-Mori-Tanaka technique; Dynamic instability; Nonlinear vibration.

Introduction

Carbon nanotubes (CNTs) were introduced three decades back by Iijima (1991). They gained enormous popularity in aerospace, civil, mechanical, and naval industries due to their potential to achieve lighter and more efficient structures. Previous studies have shown the possibility to improve strength-to-weight and stiffness-to-weight ratios as well as thermal behaviors of the plate (Gojny et al. 2004; Shi et al. 2004; Shokrieh and Rafiee 2010; Ciecierska et al. 2013; García-Macías et al. 2017; Yengejeh et al. 2017). Also, the load-carrying capacity of the plate has been shown to benefit from the use of CNTs as reinforcement (Schadler et al. 1998; Patra and Mitra 2014; Mehar and Panda 2019). Since then, a large number of investigations have been carried out. Among them, analytical and semi-analytical methods are of particular interest, as they can be successfully used for gathering insights into the additional design parameters offered by CNTs. For instance, a Navier approach was developed in Kumar and Srinivas (2017) to address vibration, buckling, and bending of a functionally graded carbon nanotubes-reinforced composite (FG-CNTRC) plate. Alternative strategies for analyzing the FG-CNTRC panel refer to the Kantorovich-Galerkin and Ritz methods, as presented in Wang et al. (2016), Kiani (2017) and Gorgeri et al. (2020) respectively.

Please, add this reference: Gorgeri, A., R. Vescovini, and L. Dozio. "Sublaminate variable kinematics shell models for functionally graded sandwich panels: Bending and free vibration response." Mechanics of Advanced Materials and Structures (2020): 1-18.

While many studies focus on static loads, real-life applications are often characterized by design requirements in the form of static and dynamic loads. In this regard, two crucial aspects are worth investigating: dynamic instability and nonlinear vibrations. Dynamic instability consists in the onset of a dynamically unstable phenomenon due to a specific combination of loading frequency, amplitude in conjunction with the natural frequencies of the members. As it concerns nonlinear vibration, the response of interest is represented by the frequency-amplitude curve of a nonlinear system excited harmonically through external forces. In the context of the first aspect, Heydarpour and Malekzadeh (2018) investigated the dynamic instability of a rotating shear deformable FG-CNTRC cylindrical shell under a uniform periodic axial load using the differential quadrature (DQ) method. They observed that the dynamic instability region shifts towards high-frequency regimes with increasing CNT volume fraction. Similar studies on the dynamic instability analysis of the FG-CNTRC plates can be found in Ke et al. (2013), Kolahchi et al. (2016), and Wu et al. (2018), where DQ is used as a solution methodology. All these studies are limited to uniform loading conditions, which is a relatively severe restrictions as loads acting on structural members of plate-like structures are generally not uniform.

Moreover, load nonuniformity may stem from the interaction with adjoining members or in the presence of partial damages at the boundaries. For this reason, it is essential to extend the capabilities of semi-analytical methods to address the dynamic instability of the CNT-reinforced composite (CNTRC) in the presence of non-uniform loadings. While a few works in the literature cover the case of dynamic instability of plates with no CNT under localized (i.e., non-uniform) in-plane periodic loadings – e.g. Deolasi and Datta (1997) and Sahu and Datta (2000), Ovesy and

Fazilati (2014), Kumar et al. (2015), Ramachandra and Panda (2012), Kumar et al. (2016b) – no previous works are available for CNTRC plates.

A second fundamental aspect with the design of plate-like structures deals with their vibration behavior: structural members may experience vibration due to periodic loadings, and their amplitude must be guaranteed not to exceed the design limit. Previous research activities are available for the free vibration response of CNT plates (Aragh et al. 2012; Yas et al. 2013; Moradi-Dastjerdi and Malek-Mohammadi 2017; Loja and Barbosa 2020), while relatively few authors have investigated their nonlinear vibration. For instance, the nonlinear vibration of the FG-CNTRC plate based on HSDT with an elastic foundation under the thermal environment was studied using different solution methodologies such as the Galerkin method (Wang and Shen 2011) and improved perturbation technique (Thanh et al. 2017). No previous studies are available on the nonlinear vibration of the CNTRC plates under non-uniform in-plane periodic excitations. Also, the effect of CNT agglomeration models and CNT mass fraction on the dynamic instability and nonlinear vibration of the CNT-reinforced composite plates are unavailable.

The scope of this work is to present a novel semi-analytical approach is to fill some of the existing gaps in the dynamic analysis of the RD-CNTRC plates. Specifically, the focus of this study is the development of a semi-analytical approach for the dynamic instability and nonlinear vibration of the RD-CNTRC plates under the action of localized in-plane periodic loadings. The formulation presented herein covers the current gap in the literature and allows us to gather a further understanding of the mechanical response of CNTRC plate-like structures. The the paper is organized as follows: the mathematical formulation is presented first, which consist of Fourier expansion of the localized in-plane loadings, estimation of the effective properties of the RD-CNTRC plate, in-plane elasticity problem, kinematics of the RD-CNTRC plate, governing partial differential equations, Galerkin method and followed by dynamic instability and nonlinear vibration analyses. Results and discussion are then presented: validation studies are conducted against Abaqus simulations and results from the literature, while parametric studies are presented to illustrate the potential of the formulation developed here.

Mathematical Formulation

Subjects of the investigation are plates characterized by randomly distributed carbon nanotube-reinforced composite (RD-CNTRC). The length and width of the plate are denoted as a and b, while the thickness is h. A Cartesian reference system is taken according to the sketch of Fig. 1, where loading conditions are illustrated. They are three cases of localized in-plane compressive periodic loadings in addition to the uniform one.

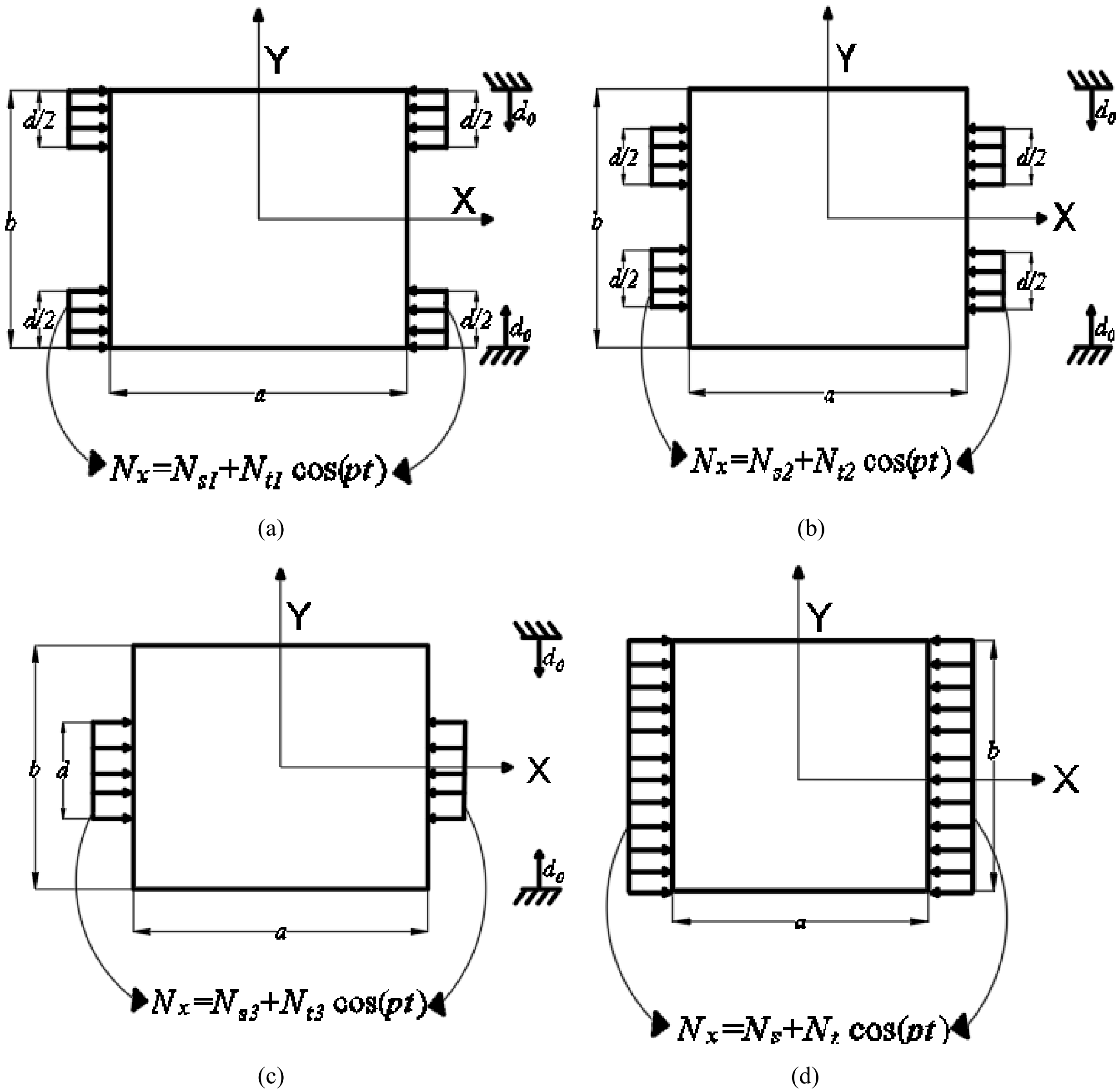

Fig. 1. Three cases of localized in-plane compressive periodic loadings, (a) Case-I, (b) Case-II, (c) Case-III, and (d) uniform periodic loading are shown.

The localized in-plane loading is modeled using the Fourier series expansion along the *y*-direction. The generalized form of localized in-plane loading function is defined as:

$$N(y) = \frac{b}{d}\left(\bar{N}_0\frac{d}{b} + \sum_{r=1}^{\infty}\frac{2\bar{N}_0}{\pi r}\left(\frac{1}{r}sin\beta_i\left(d_0 + \frac{d}{2} - \frac{b}{2}\right) + \ sin\beta_i\left(\frac{b}{2} - d_0\right)\right)cos\beta_i y\right) \tag{1}$$

where d_0 represents the distance of the load from the top or bottom edges, and *d* denotes the total width of the loading at any edge of the plate, as shown in Fig. 1. The three load cases above can be representative of the connection between a stiffened plate and a plate without stiffener, where load transfer tends to localized. Depending on d_0, the generalized form of localized in-plane loading function is reduced into three cases:

- Case I ($d_0 = 0$):

$$N(y) = \frac{b}{d}\left(\frac{\overline{N}_0 d}{b} + \sum_{r=1}^{\infty} \frac{2\overline{N}_0}{\pi r} \; sin\beta_i \left(\frac{d}{2} - \frac{b}{2}\right) cos\beta_i y\right) \tag{2}$$

- Case II ($d_0 = 0.125b$):

$$N(y) = \frac{b}{d}\left(\overline{N}_0 \frac{d}{b} + \sum_{r=1}^{\infty} \frac{2\overline{N}_0}{\pi r} \left(\frac{1}{r} sin\beta_i \left(d_0 - \frac{3b}{8}\right) + \; sin\beta_i \frac{3b}{8}\right) cos\beta_i y\right) \tag{3}$$

- Case III ($d_0 = 0.25b$):

$$N(y) = \frac{b}{d}\left(\frac{\overline{N}_0 d}{b} + \sum_{r=1}^{\infty} \frac{2\overline{N}_0}{\pi r} \left(sin\beta_i \left(\frac{d}{2} - \frac{b}{4}\right) + \; sin\beta_i \frac{b}{4}\right) cos\beta_i y\right) \tag{4}$$

For the three cases, the total loading width at the edge of the plate is kept constant, such that different distributions share the same load resultant. This choice allows the effect of different distributions/shapes of localized in-plane loads to be assessed *ceteris paribus*. The detailed derivation of all three cases of localized in-plane loadings at the edge of the plate is given in Appendix A.

The Eshelby-Mori-Tanaka Scheme

The constituents used in the plate are single-walled carbon nanotubes (SWCNT) (chiral indices (n_0, m_0) = (10, 10)) and polymer matrix (epoxy resin). SWCNT is considered transversely isotropic (Odegard et al. 2003), and hence, five independent material properties are needed to illustrate the equations of the equivalent continuum model. These properties can be used in the form of Hill's elastic moduli (k_{CNT}, l_{CNT}, m_{CNT}, n_{CNT} and p_{CNT}) (Eshely 1957; Mori and Tanaka 1973). The polymer matrix is considered as isotropic and hence has two independent elastic constants (E_{ep} and ν_{ep}). The mechanical characterizations of the CNT embedded matrix (i.e., hybrid matrix) are estimated using Eshelby-Mori-Tanaka scheme in this present investigation. In this connection, when CNTs are randomly mixed with polymer matrix, these CNTs have a tendency to agglomerate into spherical shaped inclusions within the matrix because of low bending rigidity, high aspect ratio, and high Van der Waals forces (Daghigh and Daghigh 2018; Shaffer and Windle 1999; Shi et al. 2004; Vigolo et al. 2000). To model the agglomeration, the Mori-Tanaka technique is employed here; in fact, this technique has provisions to consider the agglomeration effect of CNTs using two different parameters α and β, respectively. The former, α, is the ratio of the volume of spherical inclusions to the total volume of the CNTs embedded in the matrix; the latter, β, is the ratio of the volume of CNTs within the inclusions to the total volume of CNTs. The agglomeration can be categorized into three cases: complete agglomeration ($\alpha<\beta$, $\beta = 1$), null agglomeration ($\alpha = 1$, $\beta = 1$), and partial agglomeration ($\alpha<\beta$, $\beta<1$), as shown in Fig. 2. The bulk and shear moduli of the CNT embedded matrix are computed with the help of the bulk and shear moduli of the CNT embedded matrix when CNTs in spherical inclusions and CNTs outside spherical inclusions, respectively. The bulk and shear moduli of the CNT embedded matrix are denoted by B_{ag}^{h} and S_{ag}^{h}, respectively, when the inclusion is spherical. In this case, they are calculated as shown in Eqs. (5) and (6). When CNTs fall outside the inclusion, the bulk and shear moduli are denoted by B_{sc}^{h} and S_{sc}^{h}, respectively, and computed as given in Eqs. (7) and (8) (Tornabene et al. 2017) .

$$B_{ag}^{h} = B_{ep} + \frac{V_r\left(\hat{c} - 3B_{ep} \cdot \hat{a}\right)\beta}{3(\alpha - V_r\beta + V_r\beta \cdot \hat{a})} \tag{5}$$

$$S_{ag}^{h} = S_{ep} + \frac{V_r\left(\hat{d} - 2S_{ep} \cdot \hat{b}\right)\beta}{3\left(\alpha - V_r\beta + V_r\beta \cdot \hat{b}\right)} \tag{6}$$

$$B_{sc}^{h} = B_{ep} + \frac{V_r(1-\beta)\left(c - 3B_{ep} \cdot \hat{a}\right)}{3(1 - \alpha - V_r(1-\beta) + V_r(1-\beta) \cdot \hat{a})} \tag{7}$$

$$S_{sc}^{h} = S_{ep} + \frac{V_r(1-\beta)\left(c - 2S_{ep} \cdot \hat{b}\right)}{2\left(1 - \alpha - V_r(1-\beta) + \mathrm{V}_r(1-\beta) \cdot \hat{b}\right)} \tag{8}$$

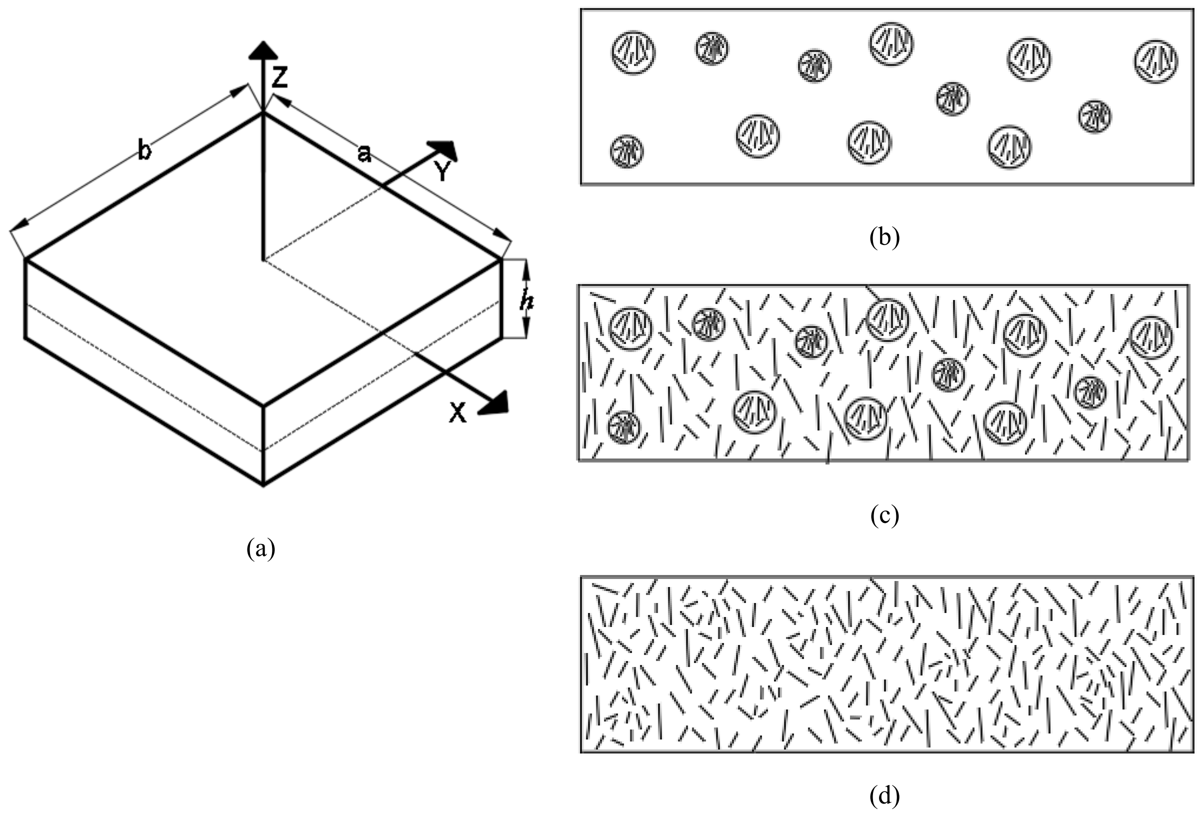

Fig. 2. (a) Schematic diagram of the RD-CNTRC plate and agglomeration models of CNTs for the randomly distributed CNTs in the matrix: (b) complete agglomeration; (c) partial agglomeration; (d) null agglomeration.

In Eqs. (5)-(8), V_r denotes the CNT volume fraction (i.e., the ratio of the volume of CNTs to the total volume of the matrix, including CNTs), and the following paramters are introduced:

$$\hat{a} = \frac{3\left(B_{ep} + S_{ep}\right) + k_{CNT} + l_{CNT}}{3\left(S_{ep} + k_{CNT}\right)} \tag{9}$$

$$\hat{b} = \frac{1}{5}\left(\frac{4S_{ep} + 2k_{CNT} + l_{CNT}}{3\left(S_{ep} + k_{CNT}\right)} + \frac{4S_{ep}}{S_{ep} + p_{CNT}} + \frac{2\left(S_{ep}\left(3B_{ep} + S_{ep}\right) + S_{ep}\left(3B_{ep} + 7S_{ep}\right)\right)}{S_{ep}\left(3B_{ep} + S_{ep}\right) + m_{CNT}\left(3B_{ep} + 7S_{ep}\right)}\right) \tag{10}$$

$$\hat{c} = \frac{1}{3}\left(n_{CNT} + 2l_{CNT} + \frac{\left(2k_{CNT} + l_{CNT}\right)\left(3B_{ep} + S_{ep} - l_{CNT}\right)}{S_{ep} + k_{CNT}}\right) \tag{11}$$

$$\hat{d} = \frac{1}{5}\left(\frac{2}{3}\left(n_{CNT} - l_{CNT}\right) + \frac{8S_{ep}p_{CNT}}{S_{ep} + p_{CNT}} + \frac{2\left(k_{CNT} - l_{CNT}\right)\left(2S_{ep} + l_{CNT}\right)}{3\left(S_{ep} + k_{CNT}\right)}\right) + \frac{1}{5}\left(\frac{8m_{CNT}S_{ep}\left(3B_{ep+}4S_{ep}\right)}{3B_{ep}\left(m_{CNT} + S_{ep}\right) + S_{ep}\left(7m_{CNT} + S_{ep}\right)}\right) \tag{12}$$

where the terms B_{ep} and S_{ep} denote the bulk and shear moduli of the matrix, respectively, defined as:.

$$B_{ep} = \frac{E_{ep}}{3\left(1 - 2\nu_{ep}\right)} \tag{13}$$

$$S_{ep} = \frac{E_{ep}}{2\left(1 + \nu_{ep}\right)} \tag{14}$$

The Poisson's ratio ν_{sc}^{h} of the CNT embedded matrix when CNTs outside spherical inclusions reads:

$$\nu_{sc}^{h} = \frac{3B_{sc}^{h} - 2S_{sc}^{h}}{6B_{sc}^{h} + 2S_{sc}^{h}} \tag{15}$$

Using Eqs. (5)-(8), and Eq. (15), the overall bulk modulus (B_{hm}) and shear modulus (S_{hm}) of the CNT embedded matrix can be computed as follows:

$$B_{hm} = B_{sc}^{h}\left(1 + \frac{\alpha\left(\frac{B_{ag}^{h}}{B_{sc}^{h}} - 1\right)}{1 + (1 - \alpha)\left(\frac{B_{ag}^{h}}{B_{sc}^{h}} - 1\right)\frac{1 + \nu_{sc}^{h}}{3 - 3\nu_{sc}^{h}}}\right) \tag{16}$$

$$S_{hm} = S_{sc}^{h}\left(1 + \frac{\alpha\left(\frac{S_{ag}^{h}}{S_{sc}^{h}} - 1\right)}{1 + (1 - \alpha)\left(\frac{S_{ag}^{h}}{S_{sc}^{h}} - 1\right)\frac{8 - 10\nu_{sc}^{h}}{15 - 15\nu_{sc}^{h}}}\right) \tag{17}$$

Using the above values of B_{hm} and S_{hm}, Young's modulus (E_{hm}) and Poisson's ratio (ν_{hm}) of the CNT embedded matrix is available as:

$$E_{hm} = \frac{9B_{hm}S_{hm}}{3B_{hm} + S_{hm}} \tag{18}$$

$$\nu_{hm} = \frac{3B_{hm} - 2S_{hm}}{6B_{hm} + 2S_{hm}} \tag{19}$$

The overall density of the CNT embedded matrix (ρ_{hm}) can be calculated using the rule of mixture (Voigt model),

$$\rho_{hm} = \rho_r V_r + \rho_{ep} V_{ep} \tag{20}$$

where the sum of volume fraction of CNT and epoxy is equal to 1 (i.e., $V_r + V_{ep} = 1$), and volume fraction of CNT is calculated by Eq. (21) using the values of given density of CNT and epoxy (i.e., ρ_r and ρ_{ep}), and mass fraction of CNT (w_r).

$$V_r = \frac{1}{\rho_r/(w_r \rho_r) - \rho_r/\rho_{ep} + 1} \tag{21}$$

Kinematics of the RD-CNTRC Plate

In the present study, the higher-order shear deformation theory (HSDT) due to Reddy and Liu (1985) is employed. Based on the HSDT, the displacement field, following Soldatos (1991), is presented as:

$$u = u^0 - z w^0_{,x} + f(z)\phi^0_x \tag{22}$$

$$u = u^0 - z w^0_{,x} + f(z)\phi^0_x \tag{23}$$

$$w = w^0 \tag{24}$$

which guarantees shear strains to be zero at the top and the bottom of the plate. In the above equations, *u, v,* and *w* indicate the displacements of a material point (*x*, *y*), which is at a distance *z* away from the reference surface of the plate along *x*, *y*, z directions, respectively. Similarly, u^0, $v^0$and w^0 denote the displacements of the point on the reference surface along *x*, *y*, z directions, respectively. The terms ϕ^0_x and ϕ^0_y represent the net rotation of the cross-section perpendicular to *x* and *y* axes, respectively. The suffix ()$_{,x,}$ and ()$_{,y}$ symbolize the differentiation with respect to *x* and *y,* respectively. Here, $f(z) = z\left(1 - \frac{4z^2}{3h^2}\right)$. At a distance z from the neutral surface of a plate, the strain-displacement equations, including the von-Kármán nonlinearity, can be written as,

$$\varepsilon_{xx} = \varepsilon^0_{xx} - z w^0_{,xx} + f(z)\phi^0_{x,x} \tag{25}$$

$$\varepsilon_{yy} = \varepsilon^0_{yy} - z w^0_{,yy} + f(z)\phi^0_{y,y} \tag{26}$$

$$\gamma_{xy} = \gamma^0_{xy} - 2z w^0_{,xy} + f(z)\phi^0_{x,y} + f(z)\phi^0_{y,x} \tag{27}$$

$$\gamma_{xz} = u_{,z} + w_{,x} = f'(z)\phi^0_x \tag{28}$$

$$\gamma_{yz} = v_{,z} + w_{,y} = f'(z)\phi^0_y \tag{29}$$

where, ε^0_{xx}, ε^0_{yy} and γ^0_{xy} are the strains at the neutral surface of the plate defined as,

$$\varepsilon_{xx}^0 = u_{,x}^0 + \frac{1}{2}\left(w_{,x}^0\right)^2 \tag{30a}$$

$$\varepsilon_{yy}^0 = v_{,y}^0 + \frac{1}{2}\left(w_{,y}^0\right)^2 \tag{30b}$$

$$\gamma_{xy}^0 = u_{,x}^0 + v_{,y}^0 + w_{,x}^0 w_{,y}^0 \tag{30c}$$

The force resultants $\mathbf{N}^T$=$\{N_{xx}, N_{yy}, N_{xy}\}$, moment resultants $\mathbf{M}^T$=$\{M_{xx}, M_{yy}, M_{xy}\}$, additional moment resultants due to additional changes in curvatures $\mathbf{M}^{a^T}$=$\{M_{xx}^a, M_{yy}^a, M_{xy}^a\}$ and shear resultants $\mathbf{Q}^T$=$\{Q_{yz}, Q_{xz}\}$ are related respectively to the membrane strains $\boldsymbol{\varepsilon}^{\mathbf{0}^T}$=$\{\varepsilon_{xx}^0, \varepsilon_{yy}^0, \varepsilon_{xy}^0\}$, bending strains $\boldsymbol{\kappa}^T$=$\{-w_{,xx}^0, -w_{,yy}^0, -2w_{,xy}^0\}$, additional bending strains $\boldsymbol{\kappa}^{a^T}$= $\{\phi_{x,x}^0, \phi_{y,y}^0, \phi_{x,y}^0 + \phi_{y,x}^0\}$ and shear strains $\boldsymbol{\gamma}^T$=$\{\gamma_{yz}, \gamma_{xz}\}$ through the constitutive relations,

$$\mathbf{N} = \mathbf{A}\boldsymbol{\varepsilon}^{\mathbf{0}} + \mathbf{B}\boldsymbol{\kappa} + \mathbf{C}\boldsymbol{\kappa}^{a} \tag{31}$$

$$\mathbf{M} = \mathbf{B}\boldsymbol{\varepsilon}^{\mathbf{0}} + \mathbf{D}\boldsymbol{\kappa} + \mathbf{E}\boldsymbol{\kappa}^{a} \tag{32}$$

$$\mathbf{M}^{a} = \mathbf{C}\boldsymbol{\varepsilon}^{\mathbf{0}} + \mathbf{E}\boldsymbol{\kappa} + \mathbf{F}\boldsymbol{\kappa}^{a} \tag{33}$$

$$\mathbf{Q} = \mathbf{H}\boldsymbol{\gamma} \tag{34}$$

Here, bold upright letters are used to denote matrices and vectors. In the above Eqs. (31) –(34), **A** (A_{ij}, *i,j* = 1,2,6), **B** (B_{ij}, *i,j* = 1,2,6), **C** (C_{ij}, *i,j* = 1,2,6), **D** (D_{ij}, *i,j* = 1,2,6), **E** (E_{ij}, *i,j* = 1,2,6), **F** (F_{ij}, *i,j* = 1,2,6) and **H** (H_{ij}, *i,j* = 4,5) are stiffness matrices of the RD-CNTRC plate. These stiffness matrices of the RD-CNTRC plate are expressed in terms of in-plane material stiffness $\mathbf{Q}$ (Q_{ij}, *i,j* = 1,2,6) and through-thickness material stiffness $\mathbf{Q}$ (Q_{ij}, *i,j* = 4,5), as stated below,

$$\left(A_{ij}, B_{ij}, D_{ij}\right) = \int_{-h/2}^{h/2} Q_{ij}(1, z, z^2)dz \qquad (i,j) = (1,2,6) \tag{35}$$

$$\left(C_{ij}, E_{ij}, F_{ij}\right) = \int_{-h/2}^{h/2} Q_{ij}\left(1, z, f(z)\right)f(z)dz \qquad (i,j) = (1,2,6) \tag{36}$$

$$\left(H_{ij}\right) = \int_{-h/2}^{h/2} Q_{ij}f'(z)f'(z)dz \qquad (i,j) = (4,5) \tag{37}$$

where the nonzero values of Q_{ij} (*i*, *j* = 1, 2, 4, 5, 6) are expressed in terms of engineering constants of CNT embedded matrix as: MISSING NUMBER IN THE FOLLOWING EQUATION

$Q_{11} = Q_{22} = E_{hm}/(1 - {\nu_{hm}}^2)$, $Q_{12} = \nu_{hm}E_{hm}/(1 - {\nu_{hm}}^2)$, $Q_{66} = Q_{44} = Q_{55} = E_{hm}/2(1 + \nu_{hm})$.

In-plane Elasticity Problem

The evaluation of in-plane stresses due to localized loads is conducted using the well-known approach based on the Airy stress function. The equilibrium equation in terms of Airy's stress function (ϕ) is defined as (Kumar et al. 2016a):

$$\frac{\partial^4\phi}{\partial x^4} + 2\frac{\partial^4\phi}{\partial x^2\partial y^2} + \frac{\partial^4\phi}{\partial y^4} = 0 \tag{38}$$

and Airy's stress function (ϕ) is defined by:

$$\eta_{xx} = \frac{\partial^2 \phi}{\partial y^2}, \eta_{yy} = \frac{\partial^2 \phi}{\partial x^2}, \eta_{xy} = -\frac{\partial^2 \phi}{\partial x \partial y} \tag{39}$$

The in-plane stress boundary conditions at all edges of the plate of the given problem are defined as:

$$\eta_{xx}\left(\pm\frac{a}{2}, y\right) = R(y),\ \eta_{xy}\left(\pm\frac{a}{2}, y\right) = 0,\ \eta_{xy}\left(x, \pm\frac{b}{2}\right) = 0,\ \eta_{yy}\left(x, \pm\frac{b}{2}\right) = 0 \tag{40}$$

where, $R(y)$ represents different types of localized in-plane mechanical load distributions at the edge of the plate. The solution is sought by assuming the stress function in terms of series as:

$$\phi(\mathrm{x}, y) = \sum_{i=1}^{\infty} r_i(y)\cos(\alpha_i x) + \sum_{j=1}^{\infty} s_j(x)\cos(\beta_j y) + R_0 y^2 \tag{41}$$

where, $\alpha_i = 2i\pi/a$, $\beta_j = 2j\pi/b$, $r_i(y)$ and $s_j(x)$ are unknown functions in y and x, respectively. Substituting the above expression in the in-plane compatibility requirement ofEq. (38) and equating the coefficients of $\cos(\alpha_i x)$ and $\cos(\beta_j y)$ results in two ordinary differential equations in $r_i(y)$ and $s_j(x)$ respectively,

$$\frac{\partial^4 r_i(y)}{\partial y^4} - 2\alpha_i^2 \frac{\partial^2 r_i(y)}{\partial y^2} + \alpha_i^4 r_i(y) = 0 \tag{42}$$

$$\frac{\partial^4 s_j(x)}{\partial x^4} - 2\beta_j^2 \frac{\partial^2 s_j(x)}{\partial x^2} + \beta_j^4 s_j(x) = 0 \tag{43}$$

Substitution of $r_i(y) = \exp\,(\overline{\lambda_2} y)$ and $s_j(x) = \exp\,(\overline{\lambda_1} x)$ in the above equations allows the roots of the equation to be found as $\overline{\lambda_2} = \pm\alpha_{i1}, \pm\alpha_{i2}$ and $\overline{\lambda_1} = \pm\beta_{j1}, \pm\beta_{j2}$, where, $\alpha_{i1}, \alpha_{i2} = \pm\alpha_i$ and $\beta_{j1}, \beta_{j2} = \pm\beta_j$. Since the functions $r_i(y)$ and $s_j(x)$ are symmetric about y and x axes respectively, we can write

$$r_i(y) = R_i \cos h(\alpha_{i1} y) + R_i\, y\cos h(\alpha_{i2} y) \tag{44}$$

$$s_j(x) = S_j \cos h(\beta_{j1} x) + S_j\, x\cos h(\beta_{j2} x) \tag{45}$$

Substituting the expressions for $r_i(y)$ and $s_j(x)$ in Eq. (41), the expression for Airy's stress function is written as:

$$\begin{aligned}\phi\,(x, y) = &\sum_{i=1}^{\infty} \{R_{i1} \cos h(\alpha_i y) + R_{i2}\, y\cos h(\alpha_i y)\}\, cos(\alpha_i x) \\ &+ \sum_{j=1}^{\infty} \{S_{j1} \cos h(\beta_j x) + S_{j2}\, x\cos h(\beta_j x)\}\, cos(\beta_j y) + R_0 y^2\end{aligned} \tag{46}$$

The in-plane stress resultants are obtained by differentiating the stress function according to Eq. (39), thus:

$$\eta_{xx} = \sum_{i=1}^{\infty} \cos(\alpha_i x) \left(R_i \cos h(\alpha_i y) \alpha_i^{\,2} + R_{i2} y \cos h(\alpha_i y)\, \alpha_{i2}^{\,2} + 2R_{i2} \alpha_i y \cos h(\alpha_i y) \right) - \sum_{j=1}^{\infty} \cos(\beta_j y) \left(S_{j1} \cos h(\beta_j x) + S_{j2} x \cos h(\beta_j x) \right) y\, \beta_j^{\,2} + 2R_0 \tag{47}$$

$$\eta_{yy} = \sum_{i=1}^{\infty} \cos(\alpha_i x) \left(R_{i1} \cos h(\alpha_i y) + R_{i2} y \cos h(\alpha_i y) \right) x\, \alpha_i^{\,2} + \sum_{j=1}^{\infty} \cos(\beta_j y) \left(S_{j1} \cos h(\beta_j x) \beta_{j1}^{\,2} + S_{j2}\, x \cos h(\beta_j x)\, \beta_j^{\,2} + 2S_{i2} \alpha_i \cos h(\beta_j x) \right) \tag{48}$$

$$\eta_{xy} = -\sum_{i=1}^{\infty} \sin(\alpha_i x)\, \alpha_i \left(R_{i1} \sin h(\alpha_i y) \alpha_i + R_{i2} \sin h(\alpha_i y) + R_{i2}\, \alpha_i y \cos h(\alpha_i y) \right) + \sum_{j=1}^{\infty} \sin(\beta_j y) \beta_j \left(S_{i1} \sin h(\beta_j x) \beta_j + S_{i2} x \cos h(\beta_j x)\, \beta_j + S_{i2} \cos h(\beta_j x) \right) \tag{49}$$

The coefficients, $R_{i1}, R_{i2}, S_{j1}, S_{j2}$ in expressions $\eta_{xx}(x,y)$, $\eta_{yy}(x,y)$ and $\eta_{xy}(x,y)$ are determined using in-plane stress boundary conditions Eq. (40), resulting in:

$$R_{i1} = -\frac{R_{i2}}{\alpha_i} \left(\frac{b}{2} \alpha_i \cot h \frac{\alpha_i b}{2} + 1 \right) \tag{50}$$

$$S_{j1} = -\frac{S_{i2}}{\beta_j} \left(\frac{a}{2} \beta_j \cot h \frac{\beta_j a}{2} + 1 \right) \tag{51}$$

$$R_{i2} = S_{j2} \beta_j \cos\frac{\beta_j b}{2} \left(\left(1 - \frac{a}{2} \beta_j \cot h \frac{\beta_j a}{2} \right) I_1 + \beta_j I_2 \right) \times \left(\frac{2/a}{\left(-\alpha_i^{\,2} \frac{b}{2} \cot h \frac{\alpha_i b}{2} - \alpha_i \right) \cos h \frac{\beta_j b}{2} + \alpha_i^{\,2} \frac{b}{2} \sin h \frac{\alpha_i b}{2}} \right) \tag{52}$$

$$S_{j2} = \left(\frac{\frac{2}{b} \cos\frac{\beta_j b}{2}}{\beta_j^{\,2} \frac{a}{2} \sin h \frac{\beta_j a}{2} - \left(\beta_j + \frac{a}{2} \beta_j^{\,2} \cot h \frac{\beta_j a}{2} \right) \cos h \frac{\beta_j a}{2}} \right) \times \left(-I_0 + \alpha_i R_{i2} \cos\frac{\alpha_i a}{2} \right) \sum_{n=1}^{\infty} \left(\left(1 - \frac{b}{2} \alpha_i \cot h \frac{\alpha_i b}{2} \right) I_3 + \alpha_i I_4 \right) \tag{53}$$

Here, $I_0 = \int_{-b/2}^{b/2} R(y) \cos(\beta_j y)\, dy$, $\quad I_1 = \int_{-a/2}^{a/2} \cos h(\beta_j x) \cos(\alpha_i x)\, dx$

$$I_2 = \int_{-a/2}^{a/2} x \sin h(\beta_j x) \cos(\alpha_i x)\, dx \qquad I_3 = \int_{-b/2}^{b/2} \cos h(\alpha_j y) \cos(\beta_i y)\, dy$$

$$I_4 = \int_{-b/2}^{b/2} y \sin h(\alpha_i y) \cos(\beta_j y)\, dy$$

Goverining Equation of Motion

Hamilton's principle Eq. (54) is used to derive the equations of motion of the RD-CNTRC plate. The variational principle reads:

$$\delta^{(1)}\left(\int_{t_0}^{t1} (U - W - T)\right) = 0 \tag{54}$$

where U is the strain energy, W is the external work done by the prescribed loads, and T is the kinetic energy in the time interval t_0 to t_1 whereas $\delta^{(1)}$ denotes the first variation. The equations of motion of the RD-CNTRC plate are then obtained as:

$$\hat{N}_{xx,x} + \hat{N}_{xy,y} = \rho_g u^0_{,tt} \tag{55}$$

$$\hat{N}_{xy,x} + \hat{N}_{yy,y} = \rho_g v^0_{,tt} \tag{56}$$

$$M_{xx,xx} + 2M_{xy,xy} + M_{yy,yy} + \left(\hat{N}_{xx} w_{,x} + \hat{N}_{xy} w_{,y}\right)_{,x} + \left(\hat{N}_{xy} w_{,x} + \hat{N}_{yy} w_{,y}\right)_{,y} = \rho_g w^0_{,tt} \tag{57}$$

$$M^a_{xx,x} + M^a_{xy,y} - Q^a_{xz} = \rho_h \phi^0_{x\,,tt} \tag{58}$$

$$M^a_{xy,x} + M^a_{yy,y} - Q^a_{yz} = \rho_h \phi^0_{y\,,tt} \tag{59}$$

In the above equations, $\rho_g = \int_{-h/2}^{h/2} \rho_{hm} dz$, $\rho_h = \int_{-h/2}^{h/2} \rho_{hm} z^2 dz$ and $\hat{N}_{ij} = [N_{ij} - n_{ij}]$, where i, j = (x, y) and n_{ij} are the internal stress resultants due to applied localized in-plane loading, and N_{ij} are the stress resultants. Therefore, $\hat{N}_{ij}$ are the net stress resultants within the RD-CNTRC plate.

Galerkin Method

The approximate solution of the partial differential equations of Eqs. (55)-(59) is sought to referring to the Galerkin method. Due to this solution strategy, the governing equations are reduced to nonlinear ordinary differential equations in the time variable by satisfying the boundary conditions. In the present study, four sets of boundary conditions are considered, SSSS, CSCS, SCSC, and CCCC. The letter S stands for simply supported and C for clamped support. The letters indicate the boundary conditions at the edge of the plate in the anti-clockwise fashion starting from the left edge. The boundary conditions at the plate edges are:

(a) Simply supported boundary conditions at $x = -{}^{a}/_{2}$ and ${}^{a}/_{2}$

$$n_{xx} - N_{xx} = -\hat{N}_{xx},\ M^a_{xx} = M_{xx} = v^0 = w^0 = \phi^0_y = 0;\ \text{and}$$

(b) Simply supported boundary conditions at $y = -{}^{b}/_{2}$ and ${}^{b}/_{2}$

$$n_{yy} - N_{yy} = -\hat{N}_{yy}\ , M_{yy}^{a} = M_{yy} = u^{0} = w^{0} = \phi_{x}^{0} = 0$$

(c) Clamped boundary conditions at $x = -{}^{a}/_{2}$ and ${}^{a}/_{2}$

$$n_{xx} - N_{xx} = -\hat{N}_{xx}, v^{o} = w^{o} = \phi_{x}{}^{o} = \phi_{y}{}^{o} = 0;\text{ and}$$

(d) Clamped boundary conditions at $y = -{}^{b}/_{2}$ and ${}^{b}/_{2}$

$$n_{yy} - N_{yy} = -\hat{N}_{yy}\ , u^{o} = w^{o} = \phi_{x}{}^{o} = \phi_{y}{}^{o} = 0$$

Based on boundary conditions of the problem, the displacement fields are expressed as:

$$u^{0} = \sum_{m=1}^{M^*}\sum_{n=1}^{N^*} U_{mn}^{*}(t)\Theta^{1}{}_{mn}(x,y) \tag{60}$$

$$v^{0} = \sum_{m=1}^{M^*}\sum_{n=1}^{N^*} V_{mn}^{*}(t)\Theta^{2}{}_{mn}(x,y) \tag{61}$$

$$w^{0} = \sum_{m=1}^{M^*}\sum_{n=1}^{N^*} W_{mn}^{*}(t)\Theta^{3}{}_{mn}(x,y) \tag{62}$$

$$\phi_{x}^{0} = \sum_{m=1}^{M^*}\sum_{n=1}^{N^*} K_{mn}^{*}(t)\Theta^{4}{}_{mn}(x,y) \tag{63}$$

$$\phi_{y}^{0} = \sum_{m=1}^{M^*}\sum_{n=1}^{N^*} L_{mn}^{*}(t)\Theta^{5}{}_{mn}(x,y) \tag{64}$$

where $U_{mn}^{*}(t), V_{mn}^{*}(t), W_{mn}^{*}(t), K_{mn}^{*}(t)$ and $L_{mn}^{*}(t)$ are undetermined coefficients independent of spatial coordinates; $\Theta^{1}{}_{mn}(x,y), \Theta^{2}{}_{mn}(x,y), \Theta^{3}{}_{mn}(x,y), \Theta^{4}{}_{mn}(x,y)$ and $\Theta^{5}{}_{mn}(x,y)$ are the assumed trial functions satisfying the boundary conditions of the problem. The subscripts *m* and *n* represent the mode number considered along *x* and *y* directions, respectively. The total number of terms along *x* and *y* directions are denoted with M^* and N^*, respectively. It follows that the total number of terms is $5 \times M^* \times N^*$. The trial functions, which satisfy the above boundary conditions at all edges of the plate, can be expressed as:

$$\Theta^{1}{}_{mn}(x,y) = sin\left(\frac{m\pi x}{a}\right) cos\left(\frac{n\pi y}{b}\right) \tag{65}$$

$$\Theta^{2}{}_{mn}(x,y) = cos\left(\frac{m\pi x}{a}\right) sin\left(\frac{n\pi y}{b}\right) \tag{66}$$

$$\Theta^{3}{}_{mn}(x,y) = X_{m}^{lr}(y)Y_{n}^{tb}(y) \tag{67}$$

$$\Theta^4{}_{mn}(x,y) = sin\left(\frac{m\pi x}{a}\right) cos\left(\frac{n\pi y}{b}\right) \tag{68}$$

$$\Theta^5{}_{mn}(x,y) = cos\left(\frac{m\pi x}{a}\right) sin\left(\frac{n\pi y}{b}\right) \tag{69}$$

where, $X_m^{lr}(x)$ and $Y_n^{tb}(y)$ are the eigenfunctions chosen to satisfy the out-of-plane boundary conditions. Here, superscripts both *lr* and *tb* replaced with *ss,* then all the edges of the plate become simply supported (i.e., SSSS), and both *lr* and *tb* replaced with *cc* then all the edges of the plate become clamped (i.e., CCCC). If *lr* is replaced with ss and *tb* is replaced with cc, then the left and right edges of the plate becomes simply supported, and the top and bottom edges of the plate becomes clamped (i.e., SCSC); the same considerations apply for the CSCS case.

The beam functions for the simply supported and clamped support at two opposite edges are:

a. Simply supported at *x* = *-a/2* and *x* = *a/2*

$$X_m^{ss}(x) = \cos\frac{m\pi x}{a} \qquad (m = 1,2,3.\ldots.) \tag{70}$$

b. Clamped support along two opposite edges, i.e., at *x* = *-a/2* and *x* = *a/2*

$$X_m^{cc}(x) = cos\,\xi_m\frac{x}{a} + \frac{sin\frac{\xi_m}{2}}{sinh\frac{\xi_m}{2}}cosh\,\xi_m\frac{x}{a} \qquad (m = 2,4,6.\ldots.) \tag{71}$$

where, ξ_m are the roots of the equation

$$tan\frac{\xi_m}{2} + tanh\frac{\xi_m}{2} = 0 \tag{72}$$

and

$$X_m^{cc}(x) = sin\,\xi_m\frac{x}{a} - \frac{sin\frac{\xi_m}{2}}{sinh\frac{\xi_m}{2}}sinh\,\xi_m\frac{x}{a} \quad (m = 3,5,7.\ldots.) \tag{73}$$

where, ξ_m are obtained as roots of the equation,

$$tan\frac{\xi_m}{2} - tanh\frac{\xi_m}{2} = 0 \tag{74}$$

The function of $Y_n(y)$ are similarly chosen based on the condition at *y* = *-b/2* and *y* = *b/2* by replacing *x* by *y* and *a* by *b* and *m* by *n* in the above equations. Galerkin method implies that:

$$\iint_A L_i(u^o,\ v^o,\ w^o, \phi_x^0, \phi_y^0)\ \Theta^i{}_{mn}(x,y)_j dxdy = 0 \text{ for } i = 1,2,3,4,5 \text{ and } j = 1,2,\ldots M^* \times N^* \tag{75}$$

where L_i is the operator expressing the nonlinear partial differential equations. The expressions for the nonlinear partial differential equations of the RD-CNTRC plate in terms of displacement components (u^o, v^o, w^o, ϕ_x^0, ϕ_y^0) are given in Appendix B.

Dynamic Instability

In dynamic instability analysis, the applied load is considered to be of the form $N_x = N_s + N_t\,cos(pt)$, where N_s is the static load term, N_t is the dynamic load term, and p denotes the angular excitation frequency. After dropping the nonlinear part of the stiffness matrix, the dynamic instability behavior of the plate is assessed by solving the following linear ordinary differential equation (i.e., Mathieu-Hill equation):

$$\mathbf{M}\ddot{\boldsymbol{\delta}} + (\mathbf{K}_{\mathrm{L}} - (N_S + N_t\cos pt)\mathbf{K}_{\mathrm{G}})\boldsymbol{\delta} = \mathbf{0} \qquad (76)$$

In the above Mathieu-Hill equation, $\mathbf{M}$ stands for the mass matrix, $\mathbf{K}_{\mathrm{L}}$ stands for the linear stiffness matrix, and $\mathbf{K}_{\mathrm{G}}$ stands for the geometric stiffness matrix of the plate. Bolotin's method is employed here for tracing the instability boundaries (Bolotin 1964). This method is suitable for the parametrically excited system as a boundary tracing method for constructing stability charts of an eigenvalue problem (Turhan 1998). In the above equation, static and dynamic load terms are varied as $N_S = \lambda_s N_{cr}$ and $N_t = \lambda_d N_{cr}$, such that $\lambda_s + \lambda_d \leq 1$, where N_{cr} is the global buckling load of the RD-CNTRC plate. Note that buckling loads and natural frequency are retrieved as special cases upon simplification of Eq. (76). The above linear ordinary differential has a periodic solution on the boundaries with period $2T$, and the solutionis sought in the form:

$$\delta(t) = \sum_{k=1,3,5}^{\infty}\left(a_k \sin\frac{kpt}{2} + b_k \cos\frac{kpt}{2}\right) \qquad (77)$$

By substituting the above solutions of $\delta(t)$ into Eq. (76) and equating coefficients of identical sine and cosine terms, a homogeneous algebraic equation in terms of the constants a_k and b_k is obtained. The boundaries of the instability region are found by seeking for a non-trivial solution. The upper and lower boundaries of the first-order approximation of the principal instability region and corrected principal instability region, respectively, are defined as:

$$|\mathbf{K}^* \pm 0.5\beta N_{cr}\mathbf{K}_{\mathbf{G}} \quad -0.25\mathbf{M}p_1^2| = 0 \qquad (78)$$

$$\begin{vmatrix} \mathbf{K}^* \pm 0.5\beta N_{cr}\mathbf{K}_{\mathbf{G}} & -0.5\beta N_{cr}\mathbf{K}_{\mathbf{G}} \\ -\beta N_{cr}\mathbf{K}_{\mathbf{G}} & \mathbf{K}^* - 2.25Mp_1^2 \end{vmatrix} - p_2^2 \begin{vmatrix} 0.25\mathbf{M} & 0 \\ 0 & 0 \end{vmatrix} = 0 \qquad (79)$$

where $\mathbf{K}^* = \mathbf{K}_{\mathbf{L}} - N_S\mathbf{K}_{\mathbf{G}}$.

Nonlinear Vibration

The mathematical expression of localized periodic loading can be expressed as, $N_x = N_s + N_t\cos(pt)$. Using Galerkin's method, the PDEs of the RD-CNTRC plate under localized in-plane loading is converted into nonlinear ODEs pertaining to both quadratic and cubic nonlinearities. The nonlinear ODEs are expressed as:

$$\mathbf{M}\ddot{\boldsymbol{\delta}} + (\mathbf{K}_{\mathrm{L}} + \mathbf{K}_{\mathrm{NL2}} + \mathbf{K}_{\mathrm{NL3}} - (N_S + N_t \cos pt)\mathbf{K}_{\mathrm{G}})\boldsymbol{\delta} = \mathbf{0} \tag{80}$$

where, $\mathbf{M}$, $\mathbf{K}_{\mathrm{L}}$, $\mathbf{K}_{\mathrm{NL2}}$, $\mathbf{K}_{\mathrm{NL3}}$ and $\mathbf{K}_{\mathrm{G}}$ are the mass, linear elastic stiffness, quadratic nonlinear stiffness, cubic nonlinear stiffness, and geometric stiffness matrices, respectively. In this present study, the Incremental Harmonic Balance (IHB) method (Cheung et al. (1990) is adopted to trace the nonlinear forced vibration response (frequency-amplitude curve) of the RD-CNTFRC plate. In this connection, the nondimensional time scale $\mathcal{T} = \omega t$ is introduced, allowing the nonlinear ordinary differential equations of Eq. (80) to be rewritten in the form:

$$\omega^2\mathbf{M}\ddot{\boldsymbol{\delta}} + (\mathbf{K}_{\mathrm{L}} + \mathbf{K}_{\mathrm{NL2}} + \mathbf{K}_{\mathrm{NL3}} - (N_S + N_t \cos \mathcal{T})\mathbf{K}_{\mathrm{G}})\boldsymbol{\delta} = \mathbf{0} \tag{81}$$

where the prime ($\dot{}$) denotes differentiation with respect to $\mathcal{T}$. Let $\boldsymbol{\delta_0}$ and ω_0 denote a state of vibration of Eq. (81); the neighboring state can be written by adding the corresponding increments as:

$$\boldsymbol{\delta} = \boldsymbol{\delta_0} + \boldsymbol{\Delta\delta} \;\text{ and }\; \omega = \omega_0 + \Delta\omega \tag{82}$$

Substituting Eq. (82) into Eq. (81) and eliminating the higher-order incremental terms, Eq. (83) is reduced to the linearized form as:

$$\omega_0{}^2\mathbf{M}\boldsymbol{\Delta}\ddot{\boldsymbol{\delta}} + (\mathbf{K}_{\mathrm{L}} + \mathbf{2K}_{\mathrm{NL2}} + \mathbf{3K}_{\mathrm{NL3}} - (N_s + N_t \cos \mathcal{T})\mathbf{K}_{\mathrm{G}})\boldsymbol{\Delta\delta} - (\mathbf{R_e} - 2\omega_0\mathbf{M}\ddot{\boldsymbol{\delta}}_{\mathbf{0}}\,\Delta\omega) = \mathbf{0} \tag{83}$$

whereby, $\mathbf{R_e} = -(\omega_0{}^2\mathbf{M}\ddot{\boldsymbol{\delta}}_{\mathbf{0}} + (\mathbf{K}_{\mathrm{L}} + \mathbf{K}_{\mathrm{NL2}} + \mathbf{K}_{\mathrm{NL3}} - (N_s + N_t \cos \mathcal{T})\mathbf{K}_{\mathrm{G}})\boldsymbol{\delta_0})$. The term $\mathbf{R_e}$ denotes the residual, which is different from zero unless the solution is the exact one. The approximate steady-state response of the system can be assumed as a truncated Fourier series.

$$\boldsymbol{\delta_{j0}} = \sum_{k=1}^{nc} a_{jk}\cos\left(\frac{2k-1}{2}\right)\mathcal{T} + \sum_{k=1}^{ns} b_{jk}\sin\left(\frac{2k-1}{2}\right)\mathcal{T} = \mathbf{T_c}\mathbf{A}_J, \tag{84}$$

$$\boldsymbol{\Delta\delta_j} = \sum_{k=1}^{nc} \Delta a_{jk}\cos\left(\frac{2k-1}{2}\right)\mathcal{T} + \sum_{k=1}^{ns} \Delta b_{jk}\sin\left(\frac{2k-1}{2}\right)\mathcal{T} = \mathrm{T_c}\boldsymbol{\Delta}\mathbf{A}_J, \tag{85}$$

where, $\mathbf{T_c} = \{\cos\frac{\mathcal{T}}{2}, \cos\frac{3\mathcal{T}}{2}, \ldots\ldots\ldots\ldots\cos\frac{(2nc-1)\mathcal{T}}{2}, \sin\frac{\mathcal{T}}{2}, \sin\frac{3\mathcal{T}}{2}, \ldots\ldots\ldots\sin\frac{(2ns-1)\mathcal{T}}{2}\}$,

$\mathbf{A}_J = \{a_{j1}, a_{j2}, \ldots\ldots\ldots a_{jnc}, b_{j1}, b_{j2}, \ldots\ldots\ldots b_{jns}\}^T$, $\boldsymbol{\Delta}\mathbf{A}_J = \{\Delta a_{j1}, \Delta a_{j2}, \ldots\ldots\ldots \Delta a_{jnc}, \Delta b_{j1}, \Delta b_{j2}, \ldots\ldots\ldots \Delta b_{jns}\}^T$. The *nc* and *ns* are the numbers of cosine and sine terms considered during the expansion of the Fourier series, respectively. Based on the above expressions of $\mathbf{A}$ and $\boldsymbol{\Delta}\mathbf{A}$, the vectors $\boldsymbol{\delta_0}$ and $\boldsymbol{\Delta\delta_0}$ can be represented in matrix form as:

$$\boldsymbol{\delta_0} = \mathbf{SA} \text{ and } \boldsymbol{\Delta\delta} = \mathbf{S\Delta A} \tag{86}$$

where $\mathbf{S} = \begin{bmatrix} \mathbf{T_c} & & & 0 \\ & \mathbf{T_c} & & \\ & & \ddots & \\ 0 & & & \mathbf{T_c} \end{bmatrix}$.

The final set of the nonlinear governing equations is derived upon substitution of Eq. (86) into Eq. (83) and by

$$\mathbf{K_{mc}}\boldsymbol{\Delta}\mathbf{A} = \mathbf{R} - \mathbf{R_{mc}}\Delta\omega \tag{87}$$

where,

$$\mathbf{K_{mc}} = \int_{\mathbf{0}}^{\mathbf{2\pi}} \mathbf{S^T}(\omega_0{}^2\mathbf{MS}'' + (\mathbf{K_L} + \mathbf{2K_{NL2}} + \mathbf{3K_{NL3}} - (N_s + N_t\cos\mathcal{T})\mathbf{K}_{\mathrm{G}})\mathbf{S})\, d\mathcal{T}$$

$$\mathbf{R} = -\int_{\mathbf{0}}^{\mathbf{2\pi}} \mathbf{S^T}(\omega_0{}^2\mathbf{MS}'' + (\mathbf{K_L} + \mathbf{K_{NL2}} + \mathbf{K_{NL3}} - (N_s + N_t\cos\mathcal{T})\mathbf{K}_{\mathrm{G}})\mathbf{S})\, \mathbf{A}d\mathcal{T}$$

$$\mathbf{R_{mc}} = \int_{\mathbf{0}}^{\mathbf{2\pi}} \mathbf{S^T}(2\omega_0\mathbf{MS}'')\, \mathbf{A}d\mathcal{T}$$

The Newton-Raphson method is employed for solving the set of nonlinear equations given by Eq. (87), thus allowing the frequency-amplitude response of the RD-CNTFRC plate to be traced.

Results and Discussion

The present study aims to analyze the nonlinear vibration and dynamic instability characteristics of the RD-CNTRC plate. In this section, three cases of localized in-plane edge loadings are considered along with uniform loading for evaluating the buckling, dynamic instability, and nonlinear vibration analyses of the RD-CNTRC plate. All three cases of localized in-plane loadings are considered in such a way that total loading at the edge of the plate is equal to that of the magnitude of uniform loading at the edge of the plate. The first 50 terms in Fourier series are considered to guarantee converged pre-buckling stresses (σ_{ij}, (i, j = x, y)) within the RD-CNTRC plate. To present the nonlinear vibration results (i.e., frequency-amplitude curve), plots are traced in terms of dimensionless excitation frequency (Ω) against dimensionless amplitude (w/h). Similarly, the instability region is traced in terms of Ω against dynamic load factor (λ_d).

The material properties are considered for the present study as per Tornabene et al. (2017). The Young's modulus (E_{ep}) is 2.1 GPa, Poisson's ratio (μ_{ep}) is 0.34, Mass density (ρ_{ep}) is 1150 kg/m^3 for matrix and for single-walled carbon nanotube (SWCNT) with chiral indices (n_0=m_0=10) having Hill's Elastic moduli as k_{CNT} =271 GPa, l_{CNT} =88 GPa, m_{CNT} =17 GPa, n_{CNT} =1089 GPa, p_{CNT} = 442 GPa and density is ρ_{CNT} =1400 Kg/m^3. The above-mentioned material properties of the matrix and CNT are considered throughout the study unless otherwise specified.

Validation Studies

The accuracy of the semi-analytical approach is demonstrated by comparison against finite element simulations and reference results available in the literature. In the first part of this section, the developed analytical stress fields within the RD-CNTRC plates is compared with Abqus results for three cases of localized in-plane loadings. With this purpose finite element models with S4R (IS THIS CORRECT?) elements were developed, and convergence checked after preliminary studies. In the second part, the buckling and vibration of the CNT-reinforced plate are validated with published results in the literature. Lastly, the dynamic instability and nonlinear vibration characteristics of the composite plate are validated with available literature.

Prebuckling Stress Distribution

In order to validate the developed analytical expression of stress, in Figs 3-5, the pre-buckling normal stress (σ_{xx}) distributions within a simply supported (SSSS) square RD-CNTRC plate (SSSS, *a/b*=1, *b/h*=50, *α*=*β*=1, w_r = 0.25, λ_d = 0) is shown against y/b at $x/a = 0$ and $x/a = 0.25$. The comparison against Abaqus results demonstrates close agreement for the predicted normal stress distribution, including local effects in proximity of the boundaries.

REMARK: or we report the thickness of the plate, or we report the results in nondimensional form. In the current version, results cannot be reproduted as thickness is not provided.

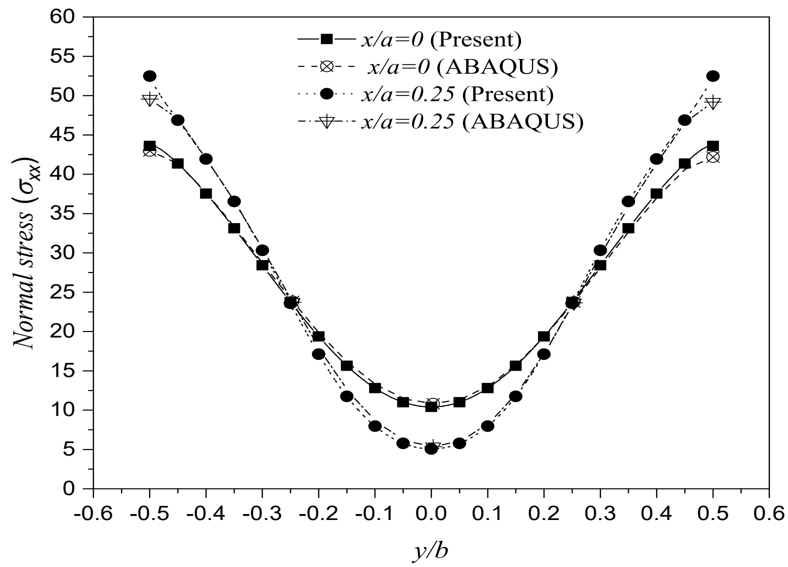

Fig. 3. Stress distribution of a simply supported square RD-CNTRC plate subjected to localized in-plane loading (Case-I)

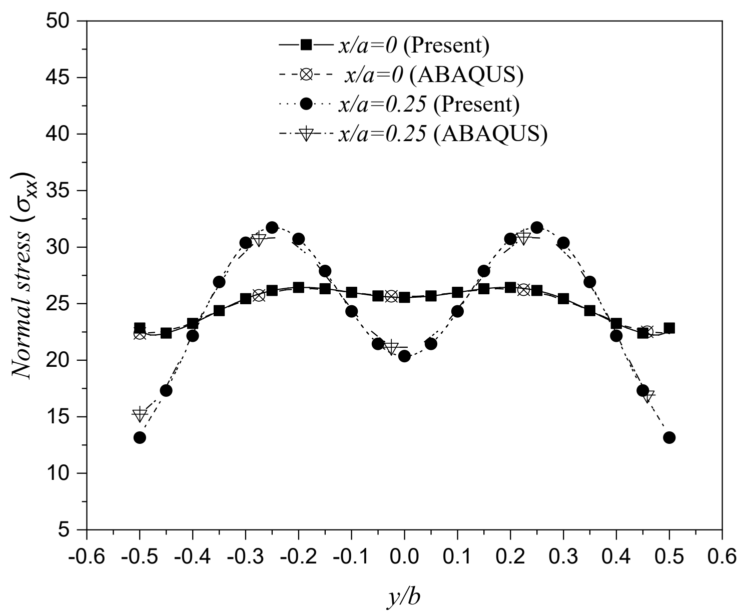

Fig. 4. Stress distribution of a simply supported square RD-CNTRC plate subjected to localized in-plane loading (Case-II)

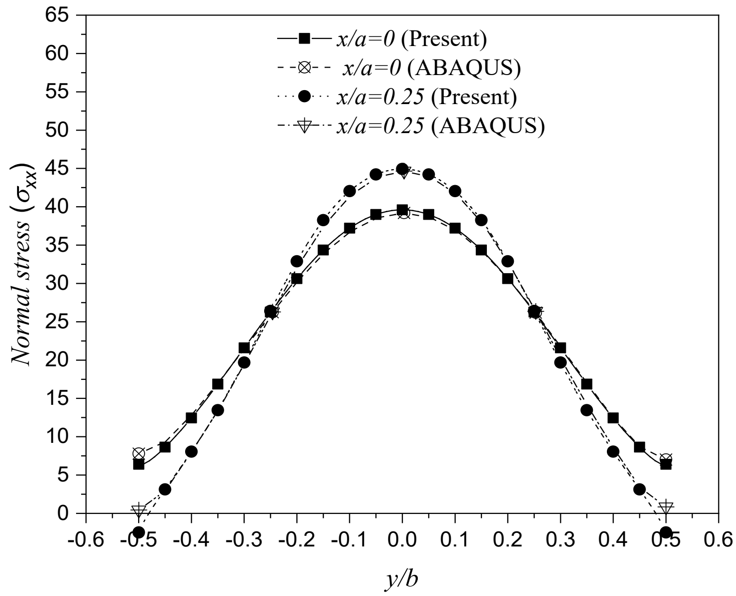

Fig. 5. Stress distribution of a simply supported square RD-CNTRC plate subjected to localized in-plane loading (Case-III)

Similarly, the contour plots of the stresses (σ_{xx}, σ_{yy}, and τ_{xy}) within a simply supported square RD-CNTRC plate (SSSS, a/b=1, b/h=50, α=β=1, w_r = 0.25, λ_d = 0) due to three cases of localized in-plane loads are obtained in ABAQUS and compared with analytically developed stress contour plots from present Airy's approach which are shown in Fig. 7-9. The plots in Figs. 6-8 indicate that the contour obtained from the current approach for all the three cases (d_0 = 0, d_0 = 0.125b, and d_0 = 0.25b) matched very well with the contours obtained in Abaqus.

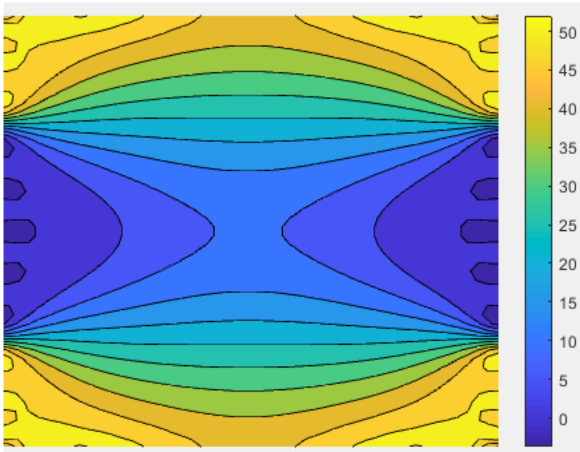

(a) Present (σ_{xx})

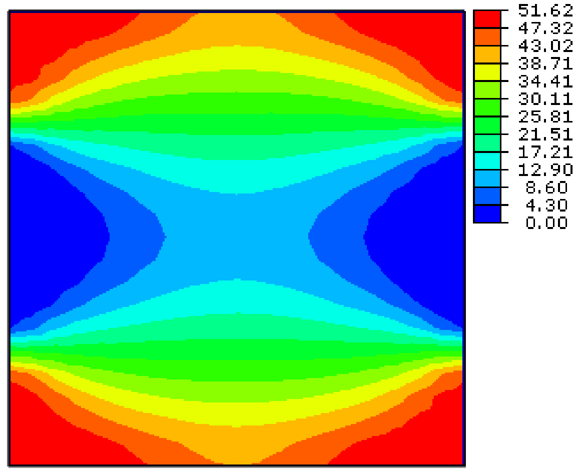

(b) ABAQUS (σ_{xx})

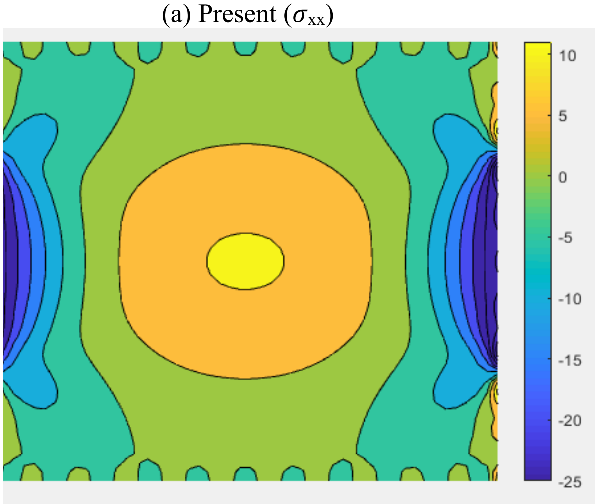

(c) Present (σ_{yy})

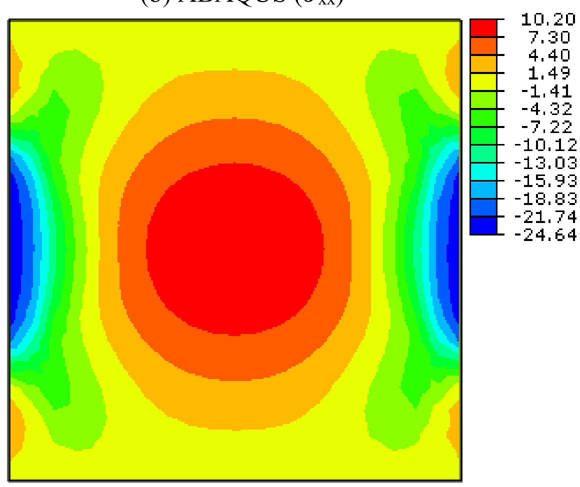

(d) ABAQUS (σ_{yy})

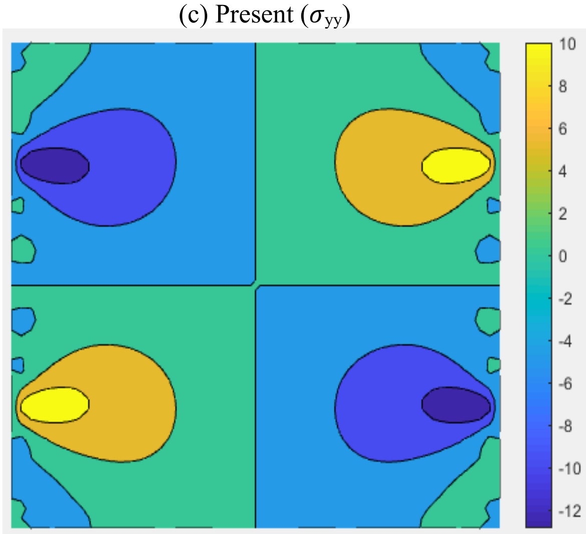

(e) Present (τ_{xy})

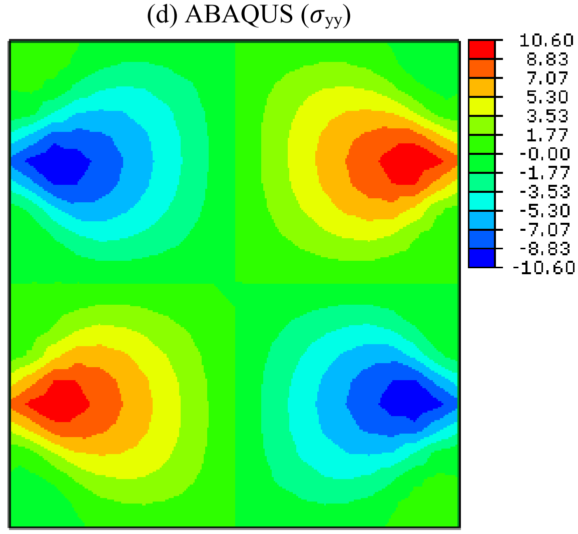

(f) ABAQUS (τ_{xy})

Fig. 6. Comparison of stress contour obtained from present method and ABAQUS of a simply supported RD-CNTRC plate ($a/b = 1$, $b/h = 50$, $\alpha = \beta = 1$, $w_r = 0.25$, $\lambda_d = 0$) for Case-I (d_0=0).

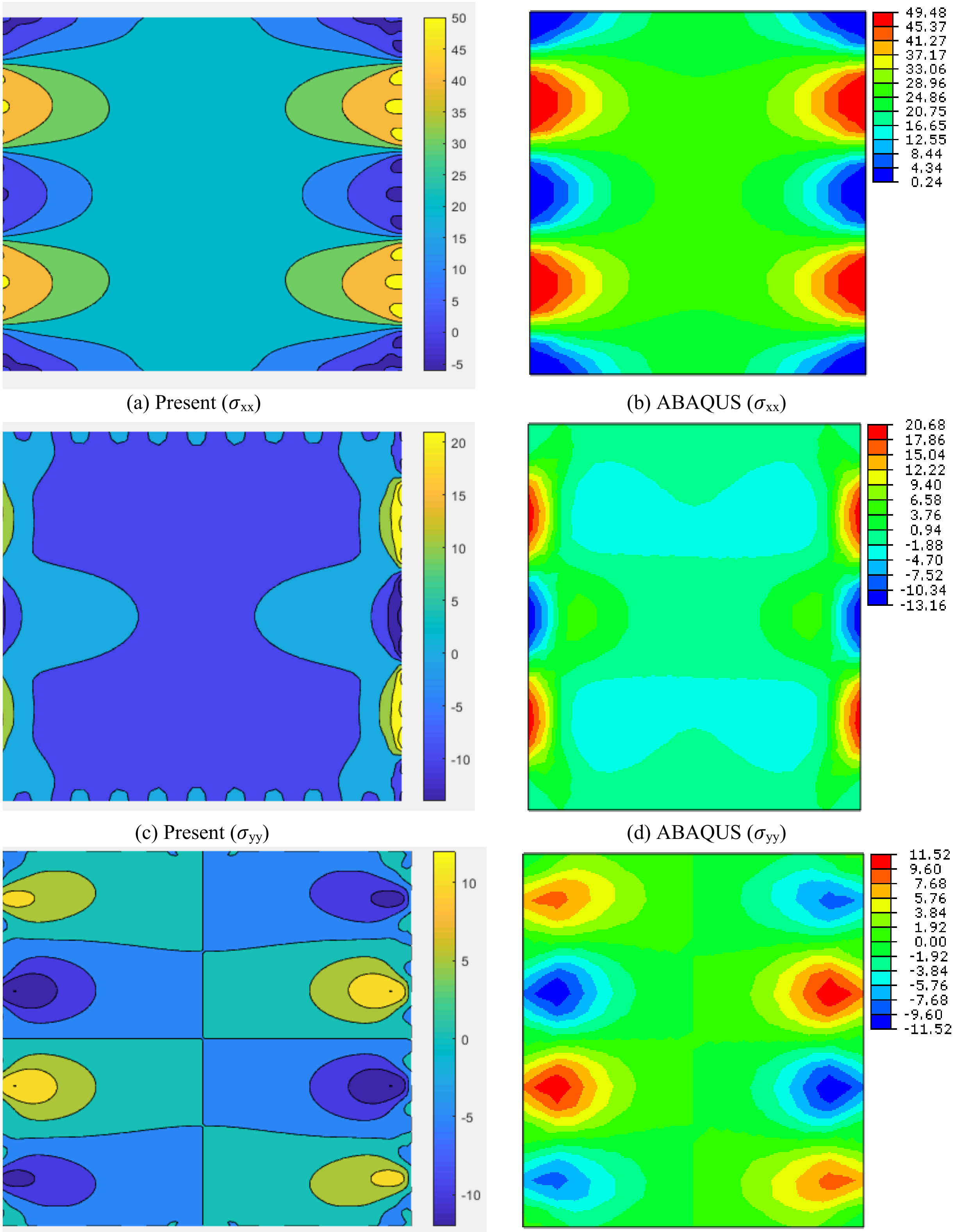

(a) Present (σ_{xx}) (b) ABAQUS (σ_{xx})

(c) Present (σ_{yy}) (d) ABAQUS (σ_{yy})

(e) Present (τ_{xy}) (f) ABAQUS (τ_{xy})

Fig. 7. Comparison of stress contour obtained from present method and ABAQUS of a simply supported RD-CNTRC plate (a/b = 1, b/h = 50, $\alpha = \beta = 1$, w_r = 0.25, λ_d = 0) for Case-II (d_0=0.125b).

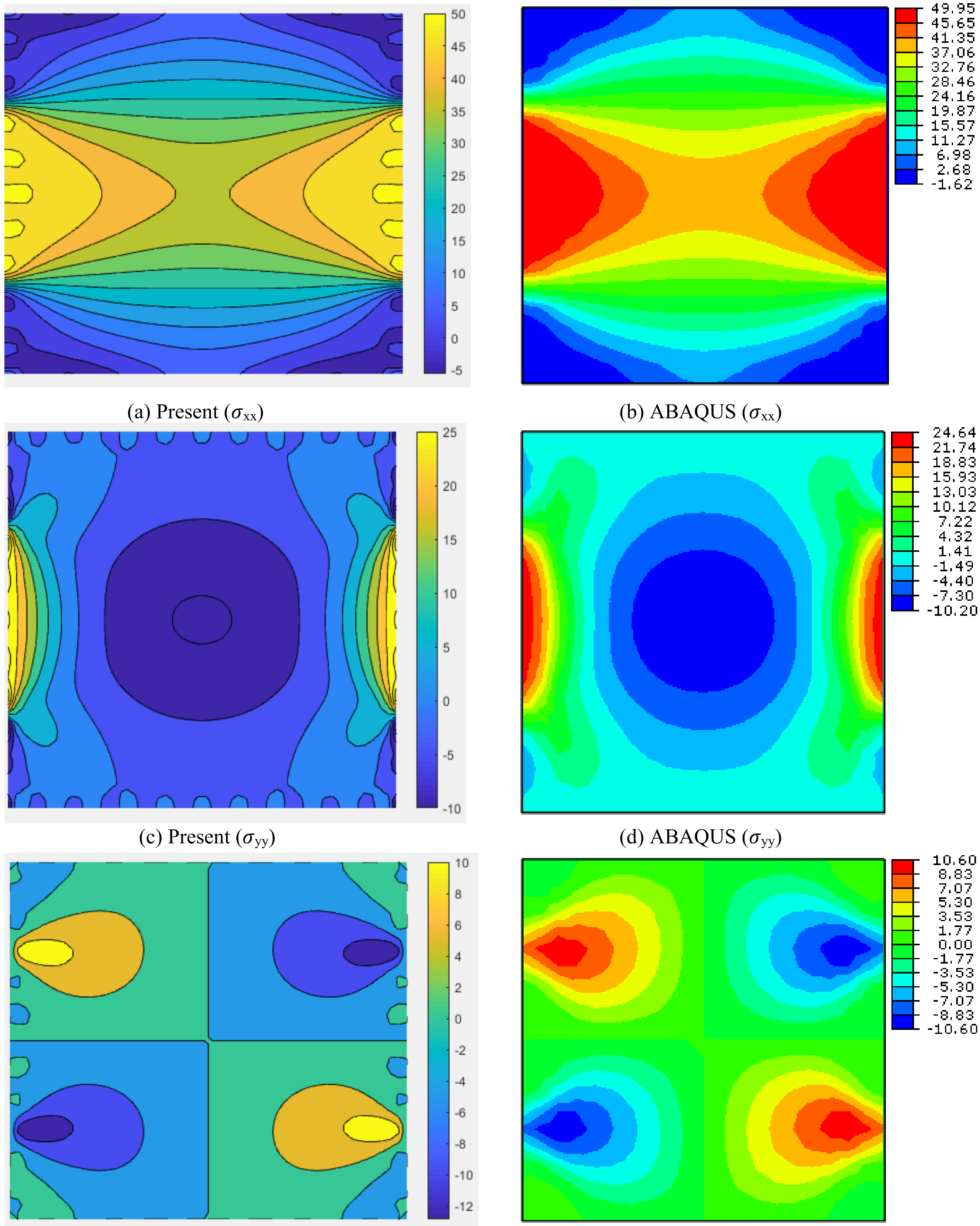

(a) Present (σ_{xx}) (b) ABAQUS (σ_{xx})

(c) Present (σ_{yy}) (d) ABAQUS (σ_{yy})

(e) Present (τ_{xy}) (f) ABAQUS (τ_{xy})

Fig. 8. Comparison of stress contour obtained from present method and ABAQUS of a simply supported RD-CNTRC plate ($a/b = 1$, $b/h = 50$, $\alpha = \beta = 1$, $w_r = 0.25$, $\lambda_d = 0$) for Case-III (d_0=0.25b).

Buckling and Vibration

HERE AND SUCCESSIVE SECTION: I would mention the techniques used in referenced papers for generating the results that we use for validation.

The nondimensional buckling load is evaluated for square, simply supported isotropic ($a/b = 1, b/h = 100, n_{12} = 0.3$) and RD-CNTRC plates (*a/b* = 1, *b/h* =20, w_r=0.25, α=β=1 and λ_d = 0) under three cases of localized in-plane loadings. The results are compared against Abaqus and benchmark solutions from the literature in Table-1. The nondimensional buckling coefficients are denoted as $k_{iso}(= \frac{\lambda_{cr} b}{D}; D = \frac{E_1 h^3}{12(1-n_{12}{}^2)})$ and $k_c \left(= \frac{\lambda_{cr} b^2}{E_{ep} h^3}\right)$ for the isotropic and RD-CNTRC plates, respectively. As seen from Table 1, close agreement is achieved between the present formulation and the results from Abaqus simulation and thise reported by Liew and Chen (2004), these latter for the localized in-plane loading case-III, only.

Table 1. Buckling load coefficient of a simply supported plate under three cases of localized in-plane loadings.

Localized in-plane loading	Dimensionless buckling coefficient				
	Isotropic plate (k_{iso})			RD-CNTRC plate (k_c)	
	Present	Abaqus	Liew and Chen (2004)	Present	Abaqus
Case-I (d_0=0)	57.05	57.14	-	116.11	116.39
Case-II (d_0=0.125*b*)	40.48	40.55	-	82.44	82.61
Case-III (d_0=0.25*b*)	30.15	30.19	30.04	61.45	61.52

Table 2. Comparison of dimensionless fundamental natural frequency ($\Omega_n = \omega_n a^2/h\sqrt{\rho_{ep}/E_{ep}}$) of a simply supported square plate (*a/b* =1) with different volume fractions of CNT and edge-thickness ratios.

b/h	$\boldsymbol{V_r}$**= 0.11**		$\boldsymbol{V_r}$ **= 0.14**		$\boldsymbol{V_r}$ **= 0.17**	
	Present	Sankar et al. (2016)	Present	Sankar et al. (2016)	Present	Sankar et al. (2016)
5	8.744	8.768	9.045	9.061	10.909	10.939
10	13.590	13.563	14.367	14.367	16.882	16.847
20	17.336	17.321	18.915	18.915	21.428	21.409
50	19.159	19.166	21.322	21.329	23.613	23.621

A further comparison against reference results is provided in terms of nondimensional natural frequency. With this purpose, a single-layered SWCNT embedded PmPv matrix, a composite square plate with different CNT volume fractions (V_r) is considered. The material properties of SWCNT are E_1^r= 5.6466 TPa, E_2^r = 7.0800 TPa, S_{12}^r = 1.9445 TPa, ρ_r = 1400 kg/m3 and ν_r = 0.175 while the PmPV matrix properties are given by Eep = 2.1 GPa, ρ_{ep} = 1150 kg/m3 and ν_{ep} = 0.34. The fundamental natural frequency (ω_n) is obtained for the above-mentioned composite plate with different CNT volume fractions and edge-thickness ratios. The nondimensional natural frequency ($\Omega_n = \omega_n a^2/h\sqrt{\rho_{ep}/E_{ep}}$) is compared in Table 2 against the results reported by Sankar et al. (2016), demonstrating close agreement with those of the semi-analytical method developed here.

Dynamic Instability and Nonlinear Vibration

To validate the present approach in terms of dynamic instability, a comparison is presented with the results reported by Adhikari and Singh (2020). Specifically, a simply supported laminated composite plate (*a/b*=1, 0/90/0) under parabolic in-plane loading is considered, and the influence of *a/h* ratio on the width of the dynamic instability region (DIR) is assessed. The material properties of the laminated composite plate are considered in this case as E_1/E_2 = 40; $G_{12}/E_2 = G_{13}/E_2$ = 0.6; G_{23}/E_2 = 0.5; υ_{12} = 0.25; ρ = 1 kg/m^3.

Here, the DIR is traced between dimensionless excitation frequency $\Omega = \omega \times \sqrt{\frac{\rho}{E_2 \times h^2}}$ vs. dynamic load factor (λ_d) and is plotted in Figure 9 for different length-to-thickness ratios. One can not the close agreement between the results obtained using the present method and the one proposed by Adhikari and Singh.

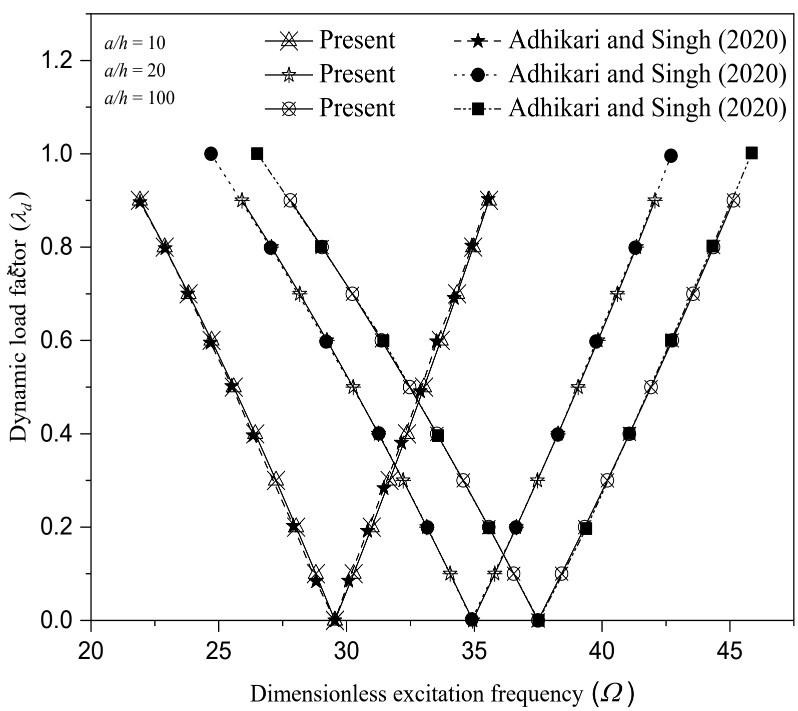

Fig. 9. Validation study of the DIR of a simply supported laminated plate (*a/b*=1, 0/90/0) with varying *a/h* ratio subjected to parabolic in-plane loading.

To investigate the accuracy and effectiveness of the present semi-analytical model for the nonlinear vibrations, the test case proposed by Ribeiro and Petyt (1999) is considered. Specifically, the material properties are E_1 = 173 GPa; E_2 = 7.2 GPa; G_{12}=G_{13}=3.76 GPa; υ_{12} = 0.29; ρ = 1540 kg/m^3. The stacking sequence consists of 16 layers of laminates with ply orientation (45/-45/0/-45/45/-45/0/45)$_s$. The plate is characterized by dimensions a = 300 mm, b =150 mm and h = 2.72 mm. Fully clamped boundary conditions are considered.

The study is conducted by considering an increasing number of trial functions up to convergence. The backbone ureves are presented in Figure 10, the results indicating that a 2-term solution is well matched with the results derived by Ribeiro and Petyt. However, these results were verified to be not converged, and increasing the basis up to 4-terms was found to be necessary. Here, the constants W_{11}, W_{13}, $W_{31,}$ and W_{33} are chosen corresponding 4-terms of w^0 displacement field and similarly, other constants are chosen for displacement fields u^0, v^0, ϕ_x^0 , and ϕ_y^0. TYPO IN THE LEGEND OF FIGURE 10 (RIBERIO→RIBEIRO)

WOULD BE INTERESTING TO FIGURE OUT WHY RIBEIRO DOES NOT REACH ACHIEVE CONVERGENCE AND TRY TO PROVIDE AN EXPLANATION

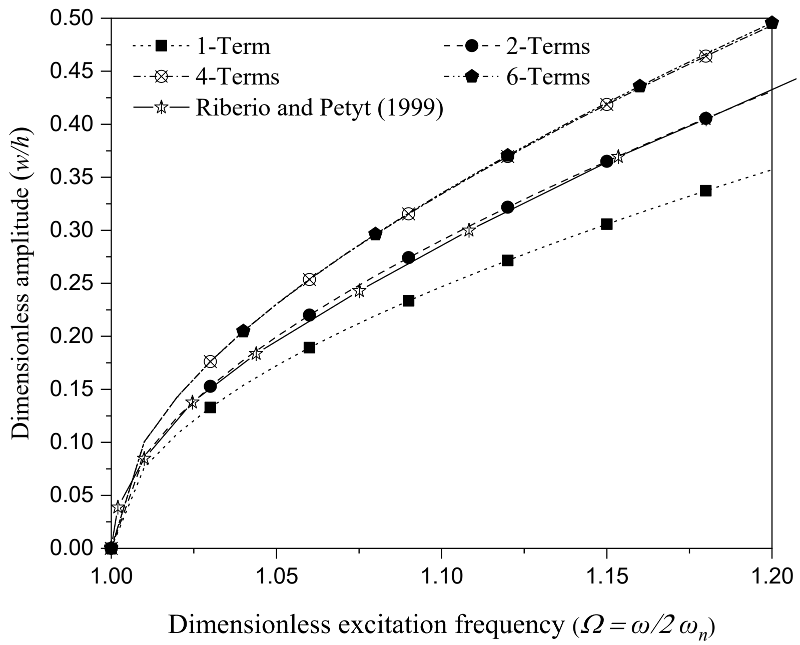

Fig. 10. Validation study of the nonlinear vibration of a fully clamped laminated rectangular plate subjected to uniform in-plane loading.

Parametric Studies

The semi-analytical tool is particularly useful for performing parametric and sensitivity studies, which are necessary for gathering understanding into the nonlinear underlying mechanical response of CNTRC plates. This feature is exploited here to address the effect of agglomeration models, static and dynamic load factors, CNT mass fraction, shape of in-plane loads, and boundary conditions.

With this purpose, a RD-CNTRC plate with an aspect ratio a/b=1 and edge-to-thickness ratio b/h=50 is considered. The material properties of the matrix and CNT are taken the same as mentioned in the initial paragraph of the results and discussion section.

Effect of Agglomeration of CNTs

The degree of agglomeration of CNTs is directly proportional to the poor dispersion of CNTs in the matrix while manufacturing the RD-CNTRC plate. As a result, the stiffness of the plate significantly reduces, and this phenomenon is consistent with findings in the existing literature. To avoid the agglomeration of CNTs for which the uniform dispersion of the CNTs in the matrix is required, which is difficult to achieve practically (I DON'T UNDERSTAND THIS SENTENCE; PLEASE REPHRASE). Hence, the study of the influence of different agglomeration models on the nonlinear vibration and dynamic instability becomes essential.

The two plots of Fig.11 illustrate the nonlinear vibration (at a dynamic load factor of λ_d = 0.5) and instability of a simply supported RD-CNTRC plate (a/b=1, b/h=50, w_r=0.25, λ_s =0) subjected to Case-III of localized in-plane loading for different agglomeration cases.

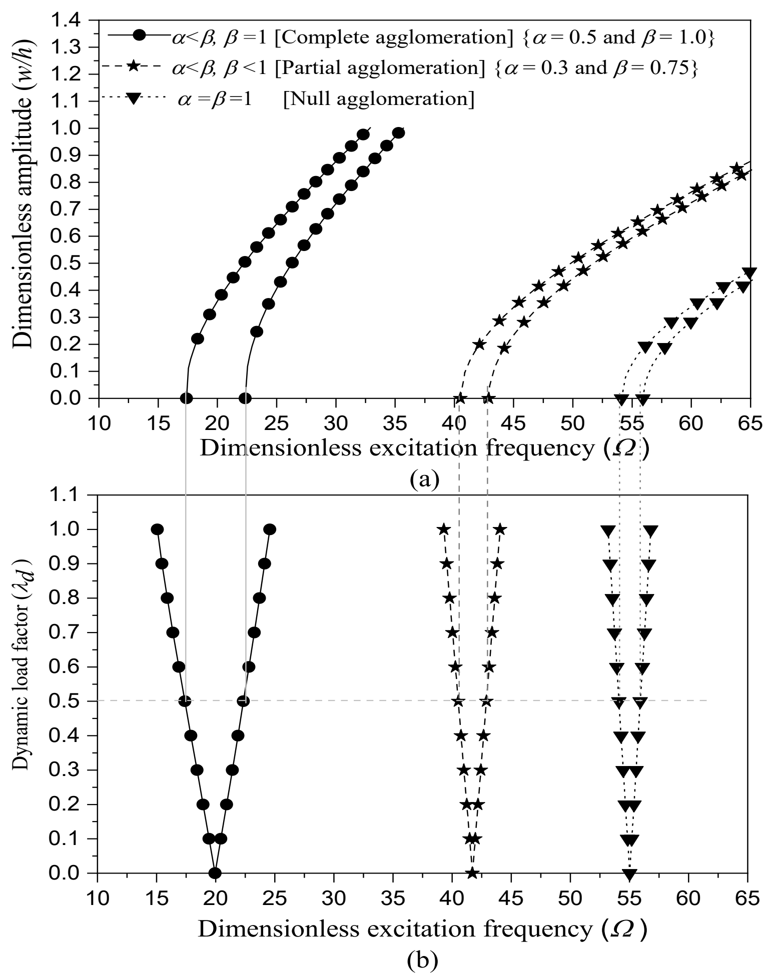

Fig. 11. Effect of CNT agglomeration on (a) nonlinear vibration response at λ_d = 0.5 and (b) principle instability zone of a simply supported RD-CNTRC plate (a/b=1, b/h=50, w_r=0.25, λ_s =0) under Case-III of localized in-plane loading.

The results of Fig. 11(a) indicates that the nonlinear behavior in the case of null agglomeration is more than (PLEASE CLARIFY) partial agglomeration, followed by a complete agglomeration case. This phenomenon occurs because the rate of change in dimensionless amplitude decreases with respect to dimensionless excitation frequency, which is due to the increase in stiffness of the plate with a decrease in agglomeration.

By inspection of Fig. 11(b), one can note that the dimensionless excitation frequency corresponding to the origin of dynamic instability is maximum for null agglomeration. In contrast, this value is minimum for the case of complete agglomeration. For the case of partial agglomeration, this behaviour depends on the value of α and β: increasing α promotes a shifts towards the null agglomeration case. The width of the instability region changes accordingly. The width of the dynamic instability region (DIR) is minimum for the null agglomeration case and maximum for the complete agglomeration case. This shows that with the increase in the agglomeration of CNTs in the matrix, the stiffness of the plate decreases and vice-versa. The sequence of the width of the dynamic instability region (DIR) for null agglomeration, partial agglomeration, and complete agglomeration as $1.80h\sqrt{E_{ep}/\rho_{ep}}$, $2.38\ h\sqrt{E_{ep}/\rho_{ep}}$ and $4.95\ h\sqrt{E_{ep}/\rho_{ep}}$ respectively at $\lambda_d = 0.5$.

The buckling load coefficient $k_c = (\lambda_{cr} b^2)/(E_{ep} h^3)$ and dimensionless natural frequency $\Omega_n = \omega_n b^2/h\sqrt{\rho_{ep}/E_{ep}}$ of a simply supported RD-CNTRC plate (a/b=1, b/h=20, w_r=0.25, λ_d =0) are summarized in Table 3. Different mass fractions and agglomeration types are considered for the three types of loading.

Table 3. Dimensionless buckling load coefficient (k_c) and dimensionless fundamental natural frequency (Ω_n) for different agglomeration models of the RD-CNTRC plate (a/b = 1, b/h =20 and λ_d = 0) subjected to three cases of localized in-plane loadings with varying mass fraction of CNT (w_r).

Type of loading	Agglomeration Type	Mass fraction							
		w_r =0		w_r =0.1		w_r =0.2		w_r =0.3	
		λ_{cr}	(Ω_n)	λ_{cr}	(Ω_n)	λ_{cr}	(Ω_n)	λ_{cr}	(Ω_n)
Case-I	CA (α= 0.5 & β= 1)	5.29	6.01	13.68	9.58	14.80	9.87	15.24	9.93
	PA (α = 0.3 & β = 0.75)	5.29	6.01	28.51	13.83	52.66	18.62	80.17	22.77
	NA (α =β = 1)	5.29	6.01	43.56	17.10	88.76	24.18	143.29	30.44
Case-II	CA (α= 0.5 & β= 1)	3.76	6.01	9.71	9.58	10.51	9.87	10.82	9.93
	PA (α = 0.3 & β = 0.75)	3.76	6.01	20.25	13.83	37.39	18.62	56.92	22.77
	NA (α =β = 1)	3.76	6.01	30.93	17.10	63.02	24.18	101.75	30.44
Case-III	CA (α= 0.5 & β= 1)	2.80	6.01	7.24	9.58	7.83	9.87	8.06	9.93
	PA (α = 0.3 & β = 0.75)	2.80	6.01	15.09	13.83	27.87	18.62	42.43	22.77
	NA (α =β = 1)	2.80	6.01	46.98	24.18	46.98	24.18	75.84	30.44

It is interesting to note that the agglomeration has a noticeable impact on the stiffness of the plate. As a consequence, the values of buckling load coefficients and dimensionless natural frequency get effected accordingly. It can be seen that with the change in agglomeration for any case of loading, suppose Case-I, when the mass fraction of CNT is changed from 0 (i.e., w_r =0), the buckling load coefficient as well as dimensionless natural frequency increases with the change in agglomeration model from complete agglomeration (CA) to partial agglomeration (PA) and then to null agglomeration (NA) (This sentence should be rephrased. It looks too involved). At the same time, it is also observed that with the change in the mass fraction of CNT in the matrix from $w_r = 0$ to $w_r = 0.3$, there is an increase in the buckling load coefficient (k_c) and dimensionless natural frequency (Ω_n). Although the rate of increase in buckling load coefficient and dimensionless natural frequency is more when CNT mass fraction (w_r) changes from 0 to 0.1, compared to CNT mass fraction changes from 0.1 to 0.3. Again, it can be concluded from table that with the change in loading case from Case-I to Case-II and then to Case-III, the values of buckling load coefficient and dimensionless natural frequency decreases for any specific agglomeration model. This shows that the loading type Case-III has a maximum effect on the RD-CNTRC plate than the other loading cases.

Effect of Pre-loading

The pre-loading at the edge of the plate can be characterized by the static load factor of the localized in-plane periodic loading. Clearly, the preload can have a beneficial or a detrimental effect on the stiffness of the plate. Tensile pre-loads stiffen the plate, while the opposite holds true for compressive ones. To investigate this effects, the nonlinear vibration and dynamic instability is assessed for a simply supported RD-CNTRC plate (a/b =1, b/h=50, α=β=1, λ_s=0, w_r = 0.25) subjected to Case-III of localized in-plane periodic loading. Firstly, the results are reported in Fig. 12 for the special case were pre-loading is null.

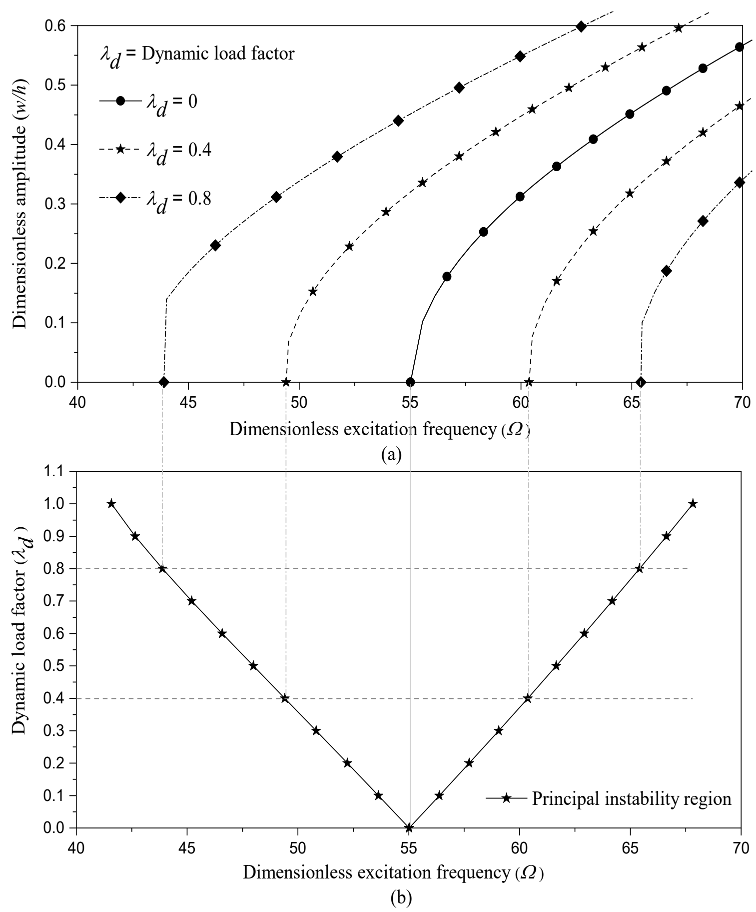

Fig. 12. Effect of dynamic load factor on (a) nonlinear vibration response at λ_d = 0, 0.4 and 0.8 and (b) principal instability zone of a simply supported RD-CNTRC plate (*a/b* =1, *b/h*=50, α=β=1, λ_s=0, w_r = 0.25) subjected to Case-III of localized in-plane loading.

The plot of Fig. 12(a) illustrates the nonlinear vibration of the RD-CNTRC plate for different dynamic load factors and width between two nonlinear vibration curves with respect to upper and lower boundaries of the principal instability region as per Fig. 12(b) at specific amplitude, increases with the increase in dynamic load factor (λ_d) (I would rephrase, this is too long). The backbone curve originates from the origin of instability corresponding to zero amplitude. Further, the amplitude increases with the increase of excitation frequency (i.e., the backbone curve shows the hardening behavior of the plate). Moreover, at any fixed value of dimensionless amplitude, the difference between upper and lower dimensionless excitation frequencies increases with the increase of dynamic load factor (λ_d) because of a decrease in the overall stiffness of the plate ($K_L + K_{Nl2} + K_{NL3} - \lambda_d N_{cr} K_G$). The influence of static load factor (i.e., pre-loading) on the nonlinear vibration response at λ_d = 0.5 and the principle instability zone of a simply supported RD-CNTRC plate (*a/b* =1, *b/h*=50, α=β=1, λ_s=0, w_r = 0.25) subjected in-plane localized loading as Case-III is shown in Fig. 13(a) and Fig. 13(b) respectively.

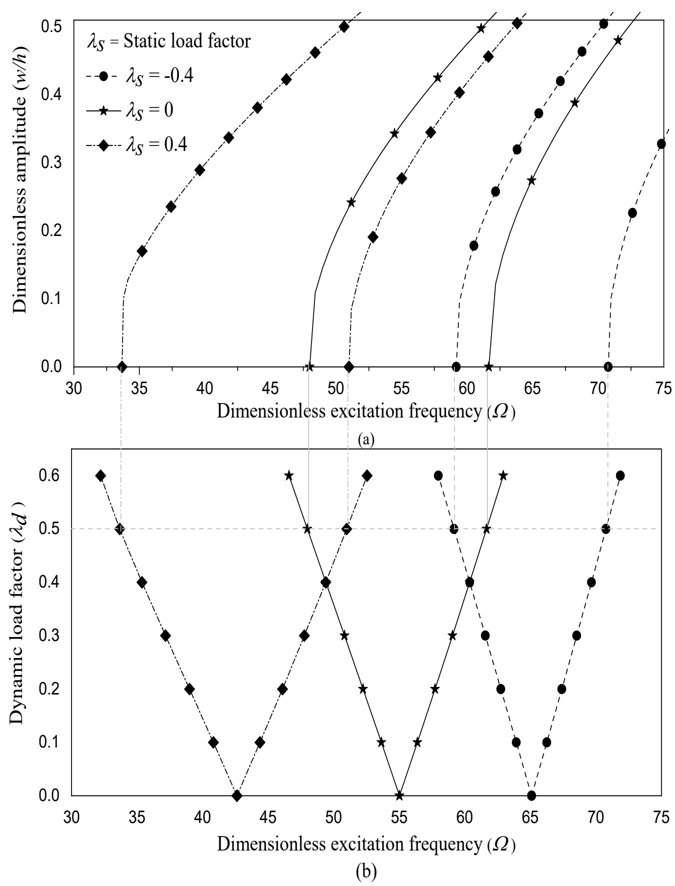

Fig. 13. Effect of static load factor on (a) nonlinear vibration response at λ_d = 0.5 and (b) principle instability zone of a simply supported RD-CNTRC plate (*a/b* =1, *b/h*=50, α=β=1, w_r = 0.25) subjected to case-III in-plane localized in-plane loading.

Fig. 13(a) shows the plot of dimensionless amplitude (w/h) vs. dimensionless excitation frequency (Ω) for different static load factors(λ_s) such as -0.4, 0, and 0.4; Where it can be observed that the increase in static load factor (λ_s) from 0 to 0.4, the stiffness of the plate decreases, which is due to compressive nature of the pre-loading effect on the plate. In contrast, stiffness increases with the decrease in static load factor (λ_s) from 0 to -0.4, which is due to the tensile nature of the pre-loading effect on the plate. Thus, the frequency-amplitude curves corresponding λ_s = 0.4 shift towards left with respect to the backbone curve corresponding to λ_s = 0, while frequency-amplitude curves corresponding to λ_s = -0.4 shift towards the right with respect to the backbone curve. From Fig. 13(b), it can be observed that the width of the dynamic instability region (DIR) is $13.67h\sqrt{E_{ep}/\rho_{ep}}$ for λ_s = 0 then increases to $17.31h\sqrt{E_{ep}/\rho_{ep}}$ for λ_s = 0.4 (due to the compressive nature of pre-loading effect on the plate which decreases its stiffness) while the width of DIR decreases to $11.59h\sqrt{E_{ep}/\rho_{ep}}$ for λ_s = -0.4 (due to tensile nature of pre-loading effect on plate which increases its stiffness) at dynamic load factor of λ_d = 0.5. Also, it is observed from the figure that the origin of instability corresponding to λ_s = 0.4 occurs at lower excitation frequency compared to the origin of instability corresponding to λ_s = 0 due to a decrease in the stiffness of the plate while the origin of instability corresponding to λ_s = -0.4 occurs at higher excitation frequency compared to the origin of instability corresponding to λ_s = 0 due to increase in the stiffness of the plate.

Effect of CNT Mass Fraction

Further paramentric studies are presented to investigate the effect of CNT mass fraction with respect to instability and the nonlinear vibration response at λ_d = 0.5. For this purpose, a simply supported RD-CNTRC plate (a/b=1, b/h=50, α=β=1, λ_s =0) subjected to Load Case-III is considered.

As observed from Fig. 14(a), the effect of nonlinearity increases with the mass fraction of CNT. In other words, the rate of increase in the amplitude of the nonlinear vibration decreases with an increase in the CNT mass fraction. One can note that the width of the dynamic instability region of the plate decreases with the increase in the mass fraction of CNTs in the matrix, as shown in Fig. 14(b). Furthermore, the origin of instability shift towards the higher value of dimensionless excitation frequency (Ω). Because of the increase in stiffness of the plate with the addition of CNTs (INCOMPLETE). The sequence of dynamic instability width for w_r=0, w_r=0.05, w_r=0.1 and w_r=0.2 at λ_d = 0.5 respectively are 3.0 $h\sqrt{E_{ep}/\rho_{ep}}$, 1.42 $h\sqrt{E_{ep}/\rho_{ep}}$, 1.04 $h\sqrt{E_{ep}/\rho_{ep}}$ and 0.72 $h\sqrt{E_{ep}/\rho_{ep}}$.

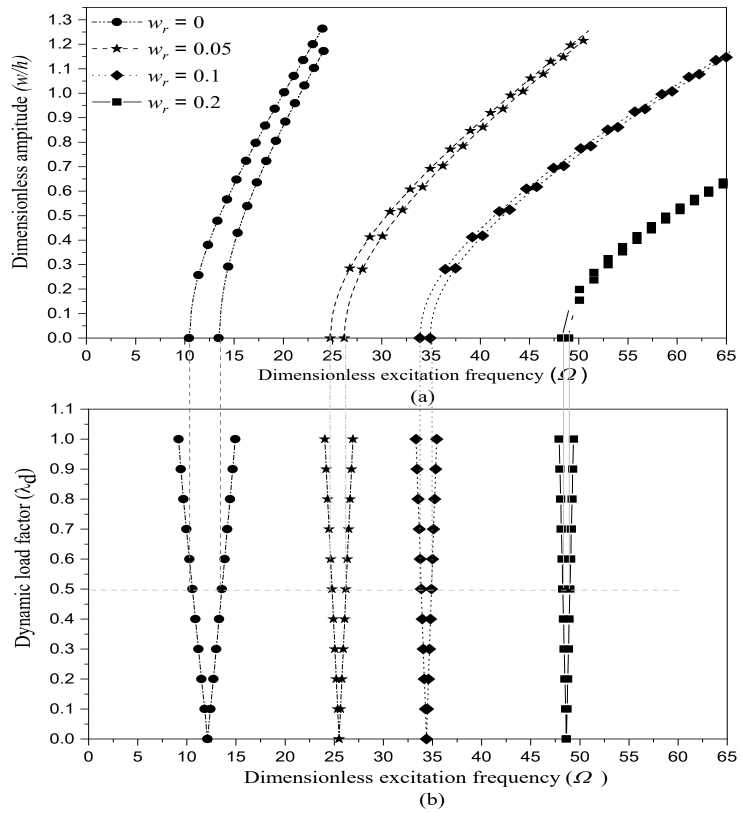

Fig. 14. Effect of CNT mass ratio (w_r) on (a) nonlinear vibration response at $\lambda_d = 0.5$ and (b) principle instability zone of a simply supported RD-CNTRC plate (a/b=1, b/h=50, α=β=1, λ_s =0) under Case-III of localized in-plane loading.

Effect of Shape of In-plane Load

In many practical situations ─ damaged boundary, stiffened plate connected to the unstiffened plate, improper connection between two structural components ─ the loads at the edge of the plate are localized. These situations can be successfully handled by using the set of in-plane loads considered in this study.

Fig. 15 reports the nonlinear vibration response at $\lambda_d = 0.5$ and the dynamic load factor of a simply supported RD-CNTRC plate (a/b=1, b/h=20, α=β=1, $\lambda_s = 0$, $w_r = 0.25$). The plate is subjected to three cases of localized and uniform in-plane loading with respect to the N_{cr} of Case-III loading. The width of the frequency-amplitude curve is maximum for Case-III loading and minimum for Case-I loading as shown in Fig. 15(a). This behavior is explained by observing that the resultant stiffness of plate ($\widehat{K} = K_L + K_{NL} \pm \lambda_d N_{cr} K_G$) for Case-III loading is less compared to the resultant stiffness associated with Case-I loading. Also, it is observed that the frequency-amplitude curve for Case-II loading and uniform loading are very close, which indicates that both the loadings have similar effects.

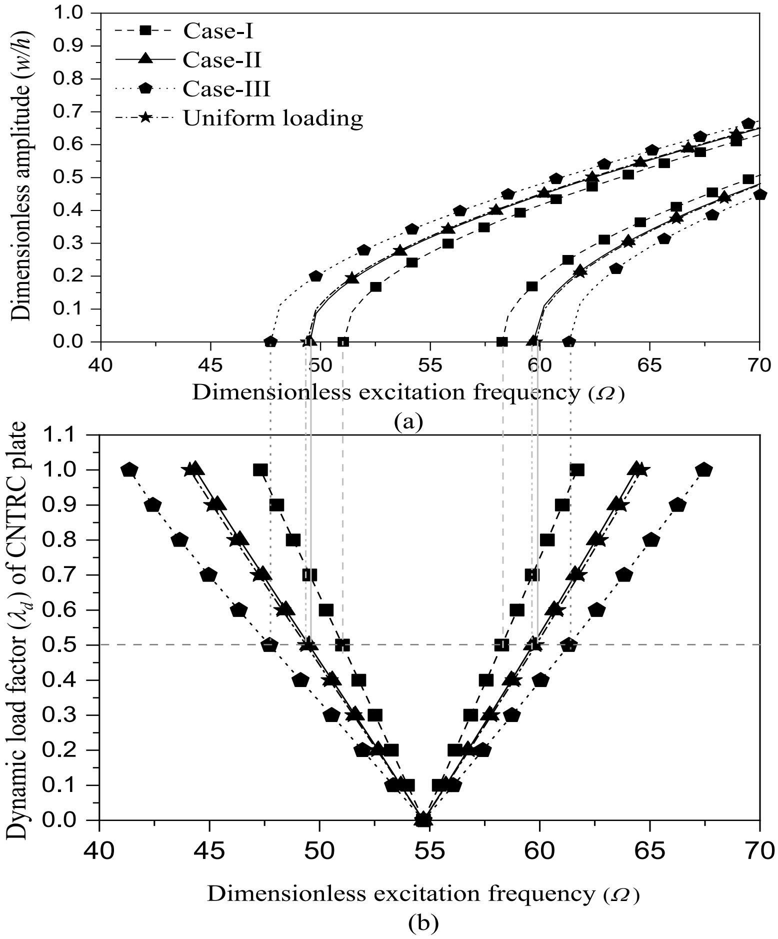

Fig. 15. (a) Nonlinear vibration response at λ_d = 0.5 and (b) principle instability zone of a simply supported RD-CNTRC plate (a/b=1, b/h=20, α=β=1, λ_s = 0, w_r = 0.25) subjected to three cases of localized in-plane loadings and uniform in-plane loading.

Similarly, from Fig. 15(b), it can be observed that the origin of the dynamic instability region for all the load cases is the same because the value of the static load factor is considered zero (λ_s = 0). However, the width of the dynamic instability region is maximum for Case-III loading and minimum for Case-I; on the contrary, for Case-II and uniform loading, it is almost the same. The sequence of dynamic instability width for Case-I, Case-II, uniform loading, and Case-III loadings are 7.22 $h\sqrt{E_{ep}/\rho_{ep}}$, 10.16 $h\sqrt{E_{ep}/\rho_{ep}}$, 10.42 $h\sqrt{E_{ep}/\rho_{ep}}$ and 13.59 $h\sqrt{E_{ep}/\rho_{ep}}$ respectively at λ_d = 0.5. This behavior is explaind by observing that the resultant stiffness of plate ($\widehat{K}$) increases in sequences as $\widehat{K}_{\text{Case-III}} < \widehat{K}_{\text{Uniform}} < \widehat{K}_{\text{Case-II}} < \widehat{K}_{\text{Case-I}}$. At λs = 0 and λ_d = 0, the initial stiffness of the plate (K_L + K_{NL1} + K_{NL2}) is independent from all the different types of loadings.

Fig. 16 reports the plot of the nonlinear vibration response at λ_d=0.5, and the dynamic instability region of a simply supported RD-CNTRC plate (a/b=1, b/h=20, α=β=1, w_r = 0.25) subjected to three cases of localized in-plane loadings and uniform in-plane loading with a static load factor of λ_s =0.4. From Fig. 16(a), it can be concluded that the nonlinear vibration response curve of the RD-CNTRC plate for Case-II loading and uniform loading the plate behaves almost the same while the nonlinear vibration response for loading Case-I and Case-III behaves differently than the other two loadings (THIS IS NOT CLEAR).

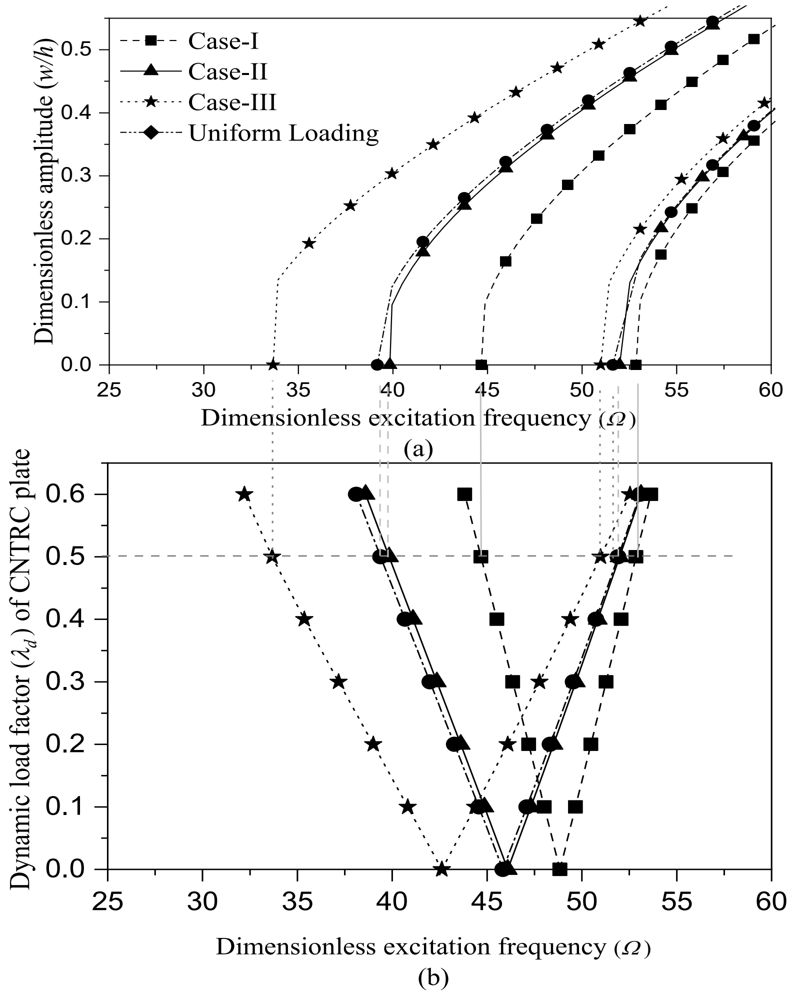

Fig. 16. (a) Nonlinear vibration response at λ_d =0.5 and (b) principle instability zone of a simply supported RD-CNTRC plate (a/b=1, b/h=20, α=β=1, λ_s =0.4, w_r = 0.25) subjected to three cases of localized in-plane loadings and uniform in-plane loading.

Also, the difference between the origin of nonlinear vibration response curves, as in Fig. 16(a) corresponding to lower and upper instability boundaries (see, Fig. 16(b)), increases with an increase in loading concentration towards the center edge of the plate. Whereas from Fig. 16(b), the origin of the dynamic instability region is not the same as it is observed in the case of Fig. 15(b). Because of the pre-loading (i.e., static load factor) applied at the edge of the plate. It is also observed from Fig. 15(b) that the Case-II loading and uniform loading has a similar effect on the instability of the RD-CNTRC plate. The sequence of dynamic instability width of RD-CNTRC plate for Case-I, Case-II, uniform, and Case-III loadings respectively are 8.17 $h\sqrt{E_{ep}/\rho_{ep}}$, 12.15 $h\sqrt{E_{ep}/\rho_{ep}}$, 12.45 $h\sqrt{E_{ep}/\rho_{ep}}$ and 17.31 $h\sqrt{E_{ep}/\rho_{ep}}$ at λ_d =0.5.

Effect of Boundary Conditions

In real-life situations, the RD-CNTRC plates can be fitted in various ways to the adjacent components of a complex structure. Hence, the effects of boundary conditions should be investigated on the nonlinear vibration and dynamic instability. For this scope. a RD-CNTRC plate (a/b=1, b/h=50, α=β=1, λ_s =0, w_r = 0.25) is considered with and different boundary conditions are analyzed. The loading condition is of the one of Case-III. The results are summarized in Fig.17.

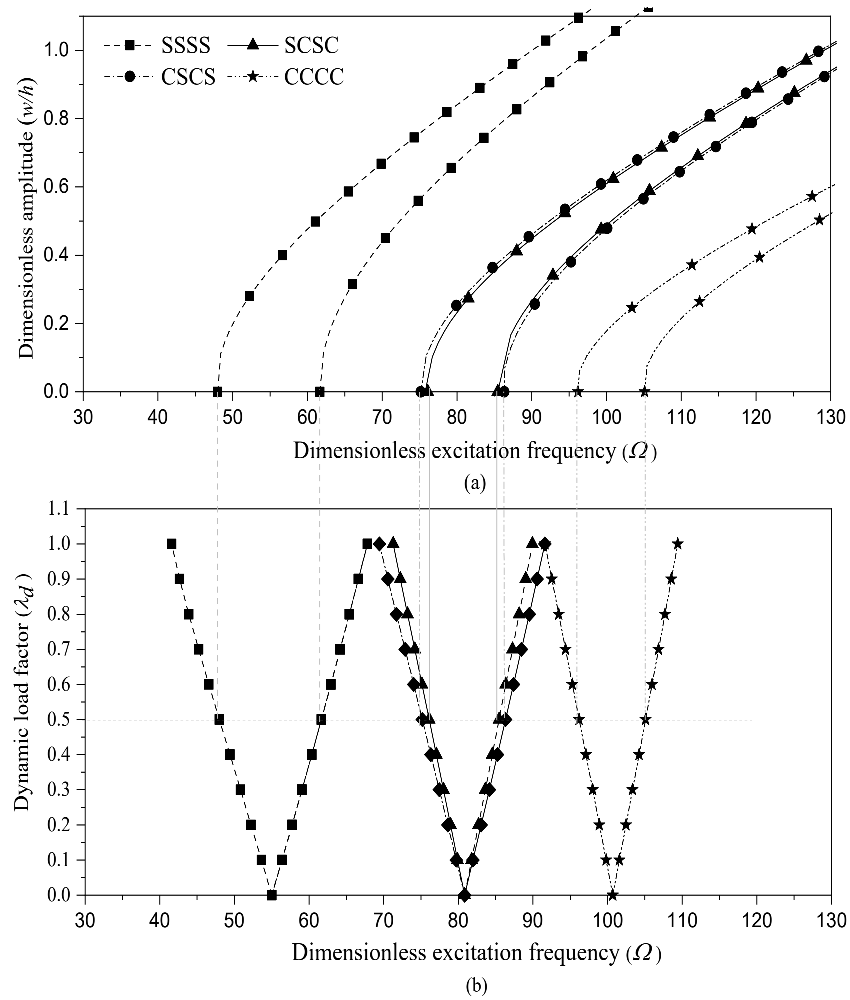

Fig. 17. (a) Nonlinear vibration response at λ_d =0.5 and (b) principle instability zone of a RD-CNTRC plate (a/b=1, b/h=50, α=β=1, λ_s =0, w_r = 0.25) with different boundary conditions subjected to Case-III of localized in-plane loading.

As seen from Fig. 17(a), SCSC and CSCS boundary conditions lead to very similar results. On the contrary, the nonlinear vibration response curves are inherently different for CCCC and SSSS conditions. As expected, fully clamped conditions promote the hardening response of the plate, as one may observe from Fig. 17(a).

Referring to Fig. 17(b), it is observed that the origin of the dynamic instability region for SCSC and CSCS boundary conditions starts from the same point of excitation frequency, whereas, for other SSSS and CCCC boundary condition, it is having a lower value and higher values respectively. Also, the dynamic instability width of the RD-

CNTRC plate with SSSS, CSCS, SCSC, and CCCC boundary conditions respectively are 13.67 $h\sqrt{E_{ep}/\rho_{ep}}$, 11.15 $h\sqrt{E_{ep}/\rho_{ep}}$, 9.36 $h\sqrt{E_{ep}/\rho_{ep}}$ and 8.91 $h\sqrt{E_{ep}/\rho_{ep}}$ at λ_d =0, which represents that the stiffness of the plate changes with the boundary condition of the plate, and thus the width of the dynamic instability region changes. Although CSCS and SCSC boundary conditions have the same origin of instability with the change in dynamic load factor, the width of the instability region changes, and it is different based on stiffness gained by the plate due to boundary conditions and which shows that SCSC condition provides more stiffness than that of CSCS condition as the width of the dynamic instability region is less for SCSC than CSCS boundary condition.

Conclusions

In this study, a semi-analytical solution has been developed to investigate the buckling, dynamic instability, and nonlinear vibration behavior of a randomly oriented SWCNT reinforced RD-CNTRC plate based on HSDT under the action of three cases of localized in-plane loadings. The effect of different types of CNT agglomeration models, CNT mass fraction, static and dynamic load factors, boundary conditions, and three cases of localized in-plane periodic loadings along with uniform loading on the dynamic instability and nonlinear vibration of the RD-CNTRC plates were studies in details. The remarks from the present semi-analytical investigation are summarized as:

- The buckling load and fundamental frequency of the RD-CNTRC plate incerase with the rise in CNT mass fraction in the matrix. However, the rate of growth in buckling loads and fundamental frequencies decreases with a further increase in CNT mass fraction compared to the case where there are no CNTs in the matrix, and CNT is added to the matrix by a small fraction.
- Pre-loading has a significant effect on the dynamic instability and nonlinear vibration of the plate. When there is no pre-load (i.e., λ_s =0), all load cases have the same origin of instability. Small increase in static load factor determine a change in the origin of instability for all load cases.
- The origin of instability shifts towards lower excitation frequency for Case-III loading and higher for Case-I type loading for any positive value of static load factor (i.e., λ_s = +ve).
- Among all the case of loadings, the width of the frequency-amplitude curve and DIR of the RD-CNTRC plate is maximum for Case-III localized loading, and minimum for Case-I localized loading. While Case-II type localized loading and uniform loading shows almost the same effect on the dynamic instability and nonlinear vibration of the RD-CNTRC plate.
- In the case of different boundary conditions, the width of the DIR of the RD-CNTRC plate is minimum for CCCC and maximum for SSSS. The plate with the CCCC boundary condition behaves more hardening than the plate with SSSS, SCSC, and CSCS boundary conditions.

Appendix A

The generalized analytical expression for the localized in-plane loading is derived using the Fourier series expansion along the *y*-direction. The loading is applied partially at the edge of the plate, so that domain of the unloaded part will be considered zero. The general case of localized in-plane loading function is written as,

$$
N(y) = \begin{cases}
0 & -\frac{b}{2} < y < -\frac{b}{2} + d_0 & \text{(A.1.1)} \\
\bar{N}_0 & -\frac{b}{2} + d_0 < y < -\frac{b}{2} + d_0 + \frac{d}{2} & \text{(A.1.2)} \\
0 & -\frac{b}{2} + d_0 + \frac{d}{2} < y < \frac{b}{2} - d_0 - \frac{d}{2} & \text{(A.1.3)} \\
\bar{N}_0 & \frac{b}{2} - d_0 - \frac{d}{2} < y < \frac{b}{2} - d_0 & \text{(A.1.4)} \\
0 & \frac{b}{2} - d_0 < y < \frac{b}{2} & \text{(A.1.5)}
\end{cases}
$$

where, d_0 is the distance from the top and the bottom of the plate edges (Fig. 18).

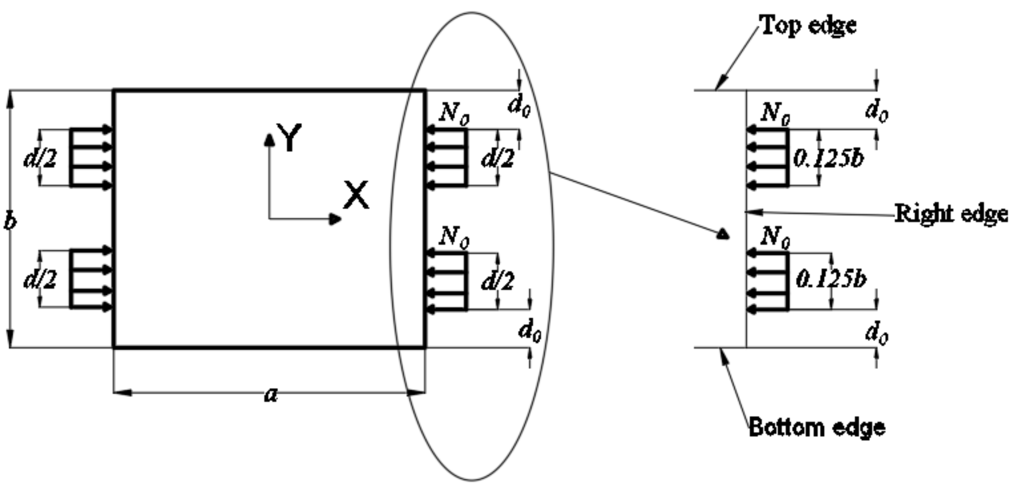

Fig. 18. Schematic diagram of RD-CNTRC plate load under localized in-plane loading representing the generalized case of loading.

The above-localized in-plane loading function is represented through Fourier series as:

$$N(y) = \frac{a_0}{2} + \sum_{i=1}^{\infty} a_i cos\beta_i y + \sum_{i=1}^{\infty} b_i sin\beta_i y \qquad \text{(A.2)}$$

where,

$$a_0 = \frac{2}{b}\left[\int_{-\frac{b}{2}}^{\frac{-b}{2}+d_0} N(y)dy + \int_{\frac{-b}{2}+d_0}^{\frac{-b}{2}+d_0+\frac{d}{2}} N(y)dy + \int_{-\frac{b}{2}+d_0+\frac{d}{2}}^{\frac{b}{2}-d_0-\frac{d}{2}} N(y)dy + \int_{\frac{b}{2}-d_0-\frac{d}{2}}^{\frac{b}{2}-d_0} N(y)dy + \int_{\frac{b}{2}-d_0}^{\frac{b}{2}} N(y)dy\right]$$

$$= \frac{2}{b}\left[\int_{\frac{-b}{2}+d_0}^{\frac{-b}{2}+d_0+\frac{d}{2}} N(y)dy + \int_{\frac{b}{2}-d_0-\frac{d}{2}}^{\frac{b}{2}-d_0} N(y)dy\right]$$

$$a_0 = \frac{2\overline{N}_0 d}{b} \qquad \text{(A.3)}$$

Again,

$$a_i = \frac{2}{b}\left[\int_{\frac{-b}{2}+d_0}^{\frac{-b}{2}+d_0+\frac{d}{2}} N(y)cos\beta_i y dy + \int_{\frac{b}{2}-d_0-\frac{d}{2}}^{\frac{b}{2}-d_0} N(y)cos\beta_i y dy\right]$$

$$= \frac{2\overline{N}_0}{\beta_i b}\left[Sin\beta_i\left(-\frac{b}{2}+d_0+\frac{d}{2}\right) - Sin\beta_i\left(-\frac{b}{2}+d_0\right) + Sin\beta_i\left(\frac{b}{2}-d_0\right) - Sin\beta_i\left(\frac{b}{2}-d_0-\frac{d}{2}\right)\right]$$

$$= \frac{4\overline{N}_0}{\beta_i b}\left[Sin\beta_i\left(\frac{d}{2}+d_0-\frac{b}{2}\right) + Sin\beta_i\left(\frac{b}{2}-d_0\right)\right]$$

Since $\beta_i = \frac{2\pi r}{b}$

$$a_i = \frac{2\overline{N}_0}{\pi r}\left[Sin\beta_i\left(\frac{d}{2}+d_0-\frac{b}{2}\right) + Sin\beta_i\left(\frac{b}{2}-d_0\right)\right] \qquad \text{(A.4)}$$

Similarly,

$$b_i = \frac{2}{b}\left[\int_{\frac{-b}{2}+d_0}^{\frac{-b}{2}+d_0+\frac{d}{2}} N(y)sin\beta_i y dy + \int_{\frac{b}{2}-d_0-\frac{d}{2}}^{\frac{b}{2}-d_0} N(y)sin\beta_i y dy\right]$$

$$= \frac{2\overline{N}_0}{\beta_i b}\left[-cos\beta_i\left(-\frac{b}{2}+d_0+\frac{d}{2}\right) + cos\beta_i\left(-\frac{b}{2}+d_0\right) - cos\beta_i\left(\frac{b}{2}-d_0\right) + cos\beta_i\left(\frac{b}{2}-d_0-\frac{d}{2}\right)\right]$$

$$= \frac{2\overline{N}_0}{\beta_i b}\left[-cos\beta_i\left(\frac{b}{2}-d_0-\frac{d}{2}\right) + cos\left(\frac{b}{2}-d_0-\frac{d}{2}\right)\right]$$

$$b_i = 0 \qquad \text{(A.5)}$$

Thus, using Eqs. (A.3), (A.4) and (A.5), Eq. (A.2) can be written as:

$$N(y) = \frac{\bar{N}_0 d}{b} + \sum_{i=1}^{\infty} \frac{2\bar{N}_0}{\pi r}\left[Sin\beta_i\left(\frac{d}{2} + d_0 - \frac{b}{2}\right) + \ Sin\beta_i\left(\frac{b}{2} - d_0\right)\right] cos\beta_i y \tag{A.6}$$

Considering, $i = r$, the generalized equation for the localized loading at the edge of the plate (keeping the total localized load to be same as uniform load) can be written as Eq. (A.7)

$$N(y) = \frac{b}{d}\left(\frac{\bar{N}_0 d}{b} + \sum_{r=1}^{\infty} \frac{2\bar{N}_0}{\pi r}\left[Sin\beta_i\left(\frac{d}{2} + d_0 - \frac{b}{2}\right) + \ Sin\beta_i\left(\frac{b}{2} - d_0\right)\right] cos\beta_i y\right) \tag{A.7}$$

Case-I: putting $d_0 = 0$ in Eq. (A.7)

$$N(y) = \frac{b}{d}\left(\frac{\bar{N}_0 d}{b} + \sum_{r=1}^{\infty} \frac{2\bar{N}_0}{\pi r}\left[Sin\beta_i\left(\frac{d}{2} - \frac{b}{2}\right) + \ Sin\beta_i\left(\frac{b}{2}\right)\right] cos\beta_i y\right)$$

Since $\beta_i = \frac{2\pi r}{b}$

$$N(y) = \frac{b}{d}\left(\frac{\bar{N}_0 d}{b} + \sum_{r=1}^{\infty} \frac{2\bar{N}_0}{\pi r}\left[Sin\beta_i\left(\frac{d}{2} - \frac{b}{2}\right)\right] cos\beta_i y\right) \tag{A.8}$$

Case-II: putting $d_0 = 0.125b$ in Eq. (A.7)

$$N(y) = \frac{b}{d}\left(\frac{\bar{N}_0 d}{b} + \sum_{r=1}^{\infty} \frac{2\bar{N}_0}{\pi r}\left[Sin\beta_i\left(\frac{d}{2} - \frac{3b}{8}\right) + \ Sin\beta_i\left(\frac{3b}{8}\right)\right] cos\beta_i y\right) \tag{A.9}$$

Case-III: putting $d_0 = 0.25b$ in Eq. (A.7)

$$N(y) = \frac{b}{d}\left(\frac{\bar{N}_0 d}{b} + \sum_{r=1}^{\infty} \frac{2\bar{N}_0}{\pi r}\left[Sin\beta_i\left(\frac{d}{2} - \frac{b}{4}\right) + \ Sin\beta_i\left(\frac{b}{4}\right)\right] cos\beta_i y\right) \tag{A.10}$$

Appendix B

The nonlinear governing partial differential equations of the RD-CNTRC plate in terms of displacements (u^0, v^0, w^0) and rotation (ϕ_x^0, ϕ_y^0) variables are given below:

$$
\begin{aligned}
&A_{11}u^0_{,xx} + 2A_{16}u^0_{,xy} + A_{66}u^0_{,yy} + A_{16}v^0_{,xx} + (A_{12} + A_{66})v^0_{,xy} + A_{26}v^0_{,yy} + A_{11}w^0_{,x}w^0_{,xx} + 2A_{16}w^0_{,x}w^0_{,xy} \\
&\quad + A_{66}w^0_{,x}w^0_{,yy} + A_{16}w^0_{,y}w^0_{,xx} + (A_{12} + A_{66})w^0_{,y}w^0_{,xy} + A_{26}w^0_{,y}w^0_{,yy} + B_{11}\phi^0_{x,xx} \\
&\quad + 2B_{16}\phi^0_{x,xy} + B_{66}\phi^0_{x,yy} + B_{16}\phi^0_{y,xx} + (B_{12} + B_{66})\phi^0_{y,xy} + B_{26}\phi^0_{y,yy} = C_g u^0_{,tt}
\end{aligned}
\tag{B.1}
$$

$$
\begin{aligned}
&A_{16}u^0_{,xx} + (A_{12} + A_{66})u^0_{,xy} + A_{26}u^0_{,yy} + A_{66}v^0_{,xx} + 2A_{26}v^0_{,xy} + A_{22}v^0_{,yy} + A_{16}w^0_{,x}w^0_{,xx} + (A_{12} \\
&\quad + A_{66})w^0_{,x}w^0_{,xy} + A_{26}w^0_{,x}w^0_{,yy} + A_{66}w^0_{,y}w^0_{,xx} + 2A_{26}w^0_{,y}w^0_{,xy} + A_{22}w^0_{,y}w^0_{,yy} \\
&\quad + B_{16}\phi^0_{x,xx} + (B_{12} + B_{66})\phi^0_{x,xy} + B_{26}\phi^0_{x,yy} + B_{66}\phi^0_{y,xx} + 2B_{26}\phi^0_{y,xy} + B_{22}\phi^0_{y,yy} \\
&\quad = C_g v^0_{,tt}
\end{aligned}
\tag{B.2}
$$

$$
\begin{aligned}
&k_c H_{55}\phi_{x,x} + k_c H_{45}\phi_{x,y} + k_c H_{45}\phi_{y,x} + k_c H_{44}\phi_{y,y} + k_c H_{55}w^0_{,xx} + k_c 2H_{45}w^0_{,xy} + k_c H_{44}w^0_{yy} \\
&\quad + (N_{xx} - (n_T)_{xx})w^0_{,xx} + 2\big(N_{xy} - (n_T)_{xy}\big)w^0_{,xy} + \big(N_{yy} - (n_T)_{yy}\big)w^0_{,yy} = \rho_g w^0_{,tt}
\end{aligned}
\tag{B.3}
$$

where,

$$
\begin{aligned}
N_{xx} = {}& A_{11}\left[u^0_{,x} + 0.5(w^0_{,x})^2\right] + A_{12}\left[v^0_{,y} + 0.5(w^0_{,y})^2\right] + A_{16}\left[u^0_{,y} + v^0_{,x} + w^0_{,x}w^0_{,y}\right] + B_{11}\phi_{x,x} + B_{12}\phi_{y,y} \\
&+ B_{16}(\phi_{x,y} + \phi_{y,x})
\end{aligned}
\tag{B.3.1}
$$

$$
\begin{aligned}
N_{yy} = {}& A_{12}\left[u^0_{,x} + 0.5(w^0_{,x})^2\right] + A_{22}\left[v^0_{,y} + 0.5(w^0_{,y})^2\right] + A_{26}\left[u^0_{,y} + v^0_{,x} + w^0_{,x}w^0_{,y}\right] + B_{12}\phi_{x,x} + B_{22}\phi_{y,y} \\
&+ B_{26}(\phi_{x,y} + \phi_{y,x})
\end{aligned}
\tag{B.3.2}
$$

$$
\begin{aligned}
N_{xy} = {}& A_{16}\left[u^0_{,x} + 0.5(w^0_{,x})^2\right] + A_{26}\left[v^0_{,y} + 0.5(w^0_{,y})^2\right] + A_{66}\left[u^0_{,y} + v^0_{,x} + w^0_{,x}w^0_{,y}\right] + B_{16}\phi_{x,x} + B_{26}\phi_{y,y} \\
&+ B_{66}(\phi_{x,y} + \phi_{y,x})
\end{aligned}
\tag{B.3.3}
$$

$$
\begin{aligned}
&B_{11}u^0_{,xx} + 2B_{16}u^0_{,xy} + B_{66}u^0_{,yy} + B_{16}v^0_{,xx} \\
&\quad + \big(B_{12} + B_{66}\big)v^0_{,xy} + B_{26}v^0_{,yy} - k_c H_{55}w^0_{,x} - k_c H_{45}w^0_{,y} + B_{11}w^0_{,x}w^0_{,xx} \\
&\quad + 2B_{16}w^0_{,x}w^0_{,xy} + B_{66}w^0_{,x}w^0_{,yy} + B_{16}w^0_{,y}w^0_{,xx} + (B_{12} + B_{66})w^0_{,y}w^0_{,xx} + B_{26}w^0_{,y}w^0_{,yy} \\
&\quad + D_{11}\phi^0_{x,xx} + 2D_{16}\phi^0_{x,xy} + D_{66}\phi^0_{x,yy} + D_{16}\phi^0_{y,xx} + (D_{12} + D_{66})\phi^0_{y,xy} + D_{26}\phi^0_{y,yy} \\
&\quad - k_c\big(H_{55}\phi_x + H_{45}\phi_y\big) = \rho_h {\phi_x}^0_{,tt}
\end{aligned}
\tag{B.4}
$$

$$
\begin{aligned}
&B_{16}u^0_{,xx} + (B_{12} + B_{66})u^0_{,xy} + B_{26}u^0_{,yy} + B_{66}v^0_{,xx} + 2B_{26}v^0_{,xy} + B_{22}v^0_{,yy} - k_c H_{45}w^0_{,x} - k_c H_{44}w^0_{,y} \\
&\quad + B_{16}w^0_{,x}w^0_{,xx} + (B_{12} + B_{66})w^0_{,x}w^0_{,xy} + B_{26}w^0_{,x}w^0_{,yy} + B_{66}w^0_{,y}w^0_{,xx} + 2B_{26}w^0_{,y}w^0_{,xy} \\
&\quad + B_{22}w^0_{,y}w^0_{,yy} + D_{16}\phi^0_{x,xx} + (D_{12} + D_{66})\phi^0_{x,xy} + D_{26}\phi^0_{x,yy} + D_{66}\phi^0_{y,yy} \\
&\quad + 2D_{26}\phi^0_{y,xy} + D_{22}\phi^0_{y,yy} - k_c(H_{45}\phi_x + H_{44}\phi_y) = \rho_h {\phi_y}^0_{,tt}
\end{aligned}
\tag{B.5}
$$

Data Availability Statement

All model and corresponding data generated and used during the present investigation appear in the published article and are available upon request.

References

Adhikari, B, and B. N. Singh. 2020. “Parametric instability analysis of laminated composite plate subject to various types of non-uniform periodic in-plane edge load.” *Applied Mathematics and Computation.* 373: 1-24.

Aragh, B. S., A. H. N. Barati, and H. Hedayati. 2012. “Eshelby-Mori-Tanaka approach for vibrational behavior of continuously graded carbon nanotube-reinforced cylindrical panels.” *Composites Part B*. 43: 1943–1954.

Bolotin, V. V. 1964. “The dynamics stabililty of elastic system.” *San Francisco, Holden day, CA*.

Cheung, Y. K., S. H. Chen, and S. L. Lau. 1990. “Application of the incremental harmonic balance method to cubic nonlinearity systems.” *Journal of Sound and Vibration*. 140(2): 273–286.

Ciecierska, E., A. Boczkowska., K. J. Kurzydlowski., I. D. Rosca, and S. V. Hoa. 2013. “The effect of carbon nanotubes on epoxy matrix nanocomposites.” *Journal of Thermal Analysis and Calorimetry*. 111: 1019–1024.

Daghigh, H., and V. Daghigh. 2018. “Free vibration of size and temperature-dependent carbon nanotube (CNT)-reinforced composite nanoplates with CNT agglomeration.” *Polymer Composites.* 1–16.

Deolasi, P. J, and P. K. Datta. 1997. “Simple and combination resonances of rectangular plates subjected to non-uniform edge loading with damping.” *Engineering Structures.* 19(12): 1011–1017.

Dey, S., T. Mukhopadhyay., S. K. Sahu, and S. Adhikari. 2018. “Stochastic dynamic stability analysis of composite curved panels subjected to non-uniform partial edge loading.” *European Journal of Mechanics, A/Solids*. 67: 108–122.

Eshely, J. D. (1957). “The determination of the elastic field of an ellipsoidal inclusion, and related problems.” *Proceedings of the Royal Society of London. Series A, Mathematical and Physical Sciences.* 241(1226): 376–396.

García-Macías, E., L. Rodríguez-Tembleque, R. Castro-Triguero, and A. Sáez. 2017. “Eshelby-Mori-Tanaka approach for post-buckling analysis of axially compressed functionally graded CNT/polymer composite cylindrical panels.” *Composites Part B: Engineering*. 128: 208–224.

Gojny, F. H., M. H. G. Wichmann, U. Köpke, B. Fiedler, and K. Schulte. 2004. “Carbon nanotube-reinforced epoxy-composites: Enhanced stiffness and fracture toughness at low nanotube content.” *Composites Science and Technology*. 64: 2363–2371.

Heydarpour, Y., and P. Malekzadeh. 2018. “Dynamic Stability of Rotating FG-CNTRC Cylindrical Shells under Combined Static and Periodic Axial Loads.” *International Journal of Structural Stability and Dynamics*. 18(12): 1–29.

Iijima, S. 1991. “Helical microtubules of graphitic carbon.” *Nature*. 354: 56–58.

Ke, L. L., J. Yang, and S. Kitipornchai, 2013. “Dynamic stability of functionally graded carbon nanotube-reinforced composite beams.” *Mechanics of Advanced Materials and Structures.* 20: 28–37.

Kiani, Y. 2017. “Buckling of FG-CNT-reinforced composite plates subjected to parabolic loading.” *Acta Mechanica*. 228: 1303–1319.

Kolahchi, R., M. Safari, and M. Esmailpour. 2016. “Dynamic stability analysis of temperature-dependent functionally graded CNT-reinforced visco-plates resting on orthotropic elastomeric medium.” *Composite Structures*. 150: 255–265.

Kumar, P., and Srinivas, J. 2017. “Vibration, buckling and bending behavior of functionally graded multi-walled carbon nanotube reinforced polymer composite plates using the layer-wise formulation.” *Composite Structures*, Elsevier Ltd, 177, 158–170.

Kumar, R., B. Banerjee, and L. S. Ramachandra. 2016a. “Nonlinear stability and dynamics of composite skew plates under nonuniform loadings using differential quadrature method.” *Mechanics Research Communication*.73: 76–90.

Kumar, R., S. C. Dutta, and S. K. Panda. 2016b. “Linear and nonlinear dynamic instability of functionally graded plate subjected to non-uniform loading.” *Composite Structures*.154: 219–230.

Kumar, R., L. S. Ramachandra, and B. Banerjee. 2015. “Dynamic instability of damped composite skew plates under non-uniform in-plane periodic loading.” *International Journal of Mechanical Sciences*. 103: 74–88.

Liew, K. M., and X. L. Chen. 2004. “Buckling of rectangular Mindlin plates subjected to partial in-plane edge loads using the radial point interpolation method.” *International Journal of Solids and Structures.* 41: 1677–1695.

Loja, M. A. R., and J. I. Barbosa. 2020. “In-plane functionally graded plates: A study on the free vibration and dynamic instability behaviours.” *Composite Structures*. 237: 1-18.

Mehar, K., and S. K. Panda. 2019. “Theoretical deflection analysis of multi-walled carbon nanotube reinforced sandwich panel and experimental verification.” *Composites Part B: Engineering*. 167: 317–328.

Moradi-Dastjerdi, R., and H. Malek-Mohammadi, 2017. “Free Vibration and Buckling Analyses of Functionally Graded Nanocomposite Plates Reinforced by Carbon Nanotube.” *Mechanics of Advanced Composite Structures.* 4(1): 59–73.

Mori, T., and K. Tanaka. 1973. “Average stress in matrix and average elastic energy of materials with misfitting inclusions.” *Acta Metallurgica*. 21: 571–574.

Odegard, G. M., T. S. Gates, K. E. Wise, C. Park, and E. J. Siochi. 2003. “Constitutive modeling of nanotube-reinforced polymer composites.” *Composites Science and Technology.* 63(11): 1671–1687.

Ovesy, H. R., and J. Fazilati. 2014. “Parametric instability analysis of laminated composite curved shells subjected to non-uniform in-plane load.” *Composite Structures*. 108: 449–455.

Patra, A., and N. Mitra. 2014. “Interface fracture of sandwich composites: Influence of MWCNT sonicated epoxy resin.” *Composites Science and Technology*. 101: 94–101.

Ramachandra, L. S., and S. K. Panda. 2012. “Dynamic instability of composite plates subjected to non-uniform in-plane loads.” *Journal of Sound and Vibration*. 331: 53–65.

Reddy J.N., C.F. Liu. 1985. A higher-order shear deformation theory of laminated elastic shells. International Journal of Engineering Science. 23(3): 319-330.

Ribeiro, P., and M. Petyt. 1999. “Multi-modal geometrical nonlinear free vibration of fully clamped composite laminated plates.” *Journal of Sound and Vibration*. 225(1): 127–152.

Sahu, S. K., and P. K. Datta. 2000. “Dynamic instability of laminated composite rectangular plates subjected to non-uniform harmonic in-plane edge loading.” *Proceedings of the Institution of Mechanical Engineers, Part G: Journal of Aerospace Engineering*. 214(5): 295–312.

Sankar, A., S. Natarajan, and M. Ganapathi. 2016. “Dynamic instability analysis of sandwich plates with CNT reinforced facesheets.” *Composite Structures*. 146: 187–200.

Schadler, L. S., S. C. Giannaris, and P. M. Ajayan. 1998. “Load transfer in carbon nanotube epoxy composites.” *Applied Physics Letters*. 73(26): 3842–3844.

Shaffer, M. S. P., and A. H. Windle. 1999. “Fabrication and Characterization of Carbon Nanotube / Poly (vinyl alcohol) Composites**.” 937–941.

Shi, D. L., X. Q., Feng, Y. Y. Huang, K. C. Hwang, and H. Gao. 2004. “The effect of nanotube waviness and agglomeration on the elastic property of carbon nanotube-reinforced composites.” *Journal of Engineering Materials and Technology, Transactions of the ASME*. 126: 250–257.

Shokrieh, M. M., and R. Rafiee. 2010. “On the tensile behavior of an embedded carbon nanotube in polymer matrix with non-bonded interphase region.” *Composite Structures*. 92: 647–652.

Soldatos, K. P. 1991. “A refined laminated plate and shell theory with applications.” *Journal of Sound and Vibration*. 144(1): 109–129.

Thanh, N. V., N. D. Khoa, N. D. Tuan, P. Tran, and N. D. Duc. 2017. “Nonlinear dynamic response and vibration of functionally graded carbon nanotube-reinforced composite (FG-CNTRC) shear deformable plates with temperature-dependent material properties and surrounded on elastic foundations.” *Journal of Thermal Stresses*. 40(10): 1254–1274.

Tornabene, F., B. Michele, N. Fantuzzi, and J. N. Reddy. 2017. “Multiscale Approach for Three-Phase CNT/Polymer/ Fiber Laminated Nanocomposite Structures.” *Polymer Composites*. 1–25.

Turhan, Ö. 1998. “A generalized Bolotin’s method for stability limit determination of parametrically excited systems.” *Journal of sound and vibration*. 216: 851–863.

Vigolo, B., A. Pénicaud, C. Coulon, C. Sauder, R. Pailler, C. Journet, P. Bernier, P. Poulin. 2000. “Macroscopic Fibers and Ribbons of Oriented Carbon Nanotubes.” 290(5495): 1331–1334.

Wang, M., Z. M. Li, and P. Qiao. 2016. “Semi-analytical solutions to buckling and free vibration analysis of carbon nanotube-reinforced composite thin plates.” *Composite Structures*. 144: 33–43.

Wang, Z. X., and H. S. Shen. 2011. “Nonlinear vibration of nanotube-reinforced composite plates in thermal environments.” *Computational Materials Science*. 50(8): 2319–2330.

Wu, H., J. Yang, and S. Kitipornchai. 2018. “Parametric instability of thermo-mechanically loaded functionally graded graphene reinforced nanocomposite plates.” *International Journal of Mechanical Sciences*. 135: 431–440.

Yas, M. H., A. Pourasghar, S. Kamarian, and M. Heshmatia. 2013. “Three-dimensional free vibration analysis of functionally graded nanocomposite cylindrical panels reinforced by carbon nanotube.” *Materials and Design*. 49: 583–590.

Yengejeh, S. I., S. A. Kazemi, and A. Öchsner. 2017. “Carbon nanotubes as reinforcement in composites: A review of the analytical, numerical and experimental approaches.” *Computational Materials Science*. 136: 85–101.